Energy-conserving Particle-In-Cell scheme based on Galerkin methods with sparse grids

Clément Guillet

ENERGY-CONSERVING PARTICLE-IN-CELL SCHEME BASED ON GALERKIN METHODS WITH SPARSE GRIDS

C. GUILLET*

Abstract. Sparse grid reconstructions have recently been applied to Particle-In-Cell (PIC) methods with a semi-implicit formulation, as demonstrated in [21], to reduce computational costs. By linearizing the particle equations and using a finite difference discretization of the field's equations, along with incorporating sparse grid reconstructions through the combination technique, an exactly energy-conserving scheme was proposed. However, this scheme exhibited numerical instability due to the loss of non-negativity in electric energy, inherent to the combination technique. This paper introduces a novel PIC method with a semi-implicit formulation that embeds sparse grid techniques to exactly conserve discrete total energy, defined as the sum of non-negative kinetic and field energies, ensuring nonlinear stability. The method utilizes a Galerkin approach for the field equations, employing a hierarchical sparse grid representation in the approximation space. This distinguishes it from previous sparse grid PIC methods, which typically use the combination technique and nodal representation. Key features of the method include: unconditional stability with respect to the plasma period; elimination of finite grid instability, allowing flexible grid discretization; exact conservation of discrete total energy; significant reduction in statistical error compared to standard grid schemes for the same number of particles; and decreased computational complexity, particularly in the size of the linear system to be solved. We validate the method through a series of two-dimensional test cases, demonstrating its numerical stability and robust performance.

Key words. Sparse grid, plasma physics, electrostatic, energy-conserving, semi-implicit, particle-in-cell

1. Introduction.

Particle-In-Cell (PIC) methods are among the most widely used numerical techniques for simulating kinetic plasmas [2, 8, 9, 18]. These methods discretize the Vlasov-Maxwell system of equations or, in the electrostatic regime, the Vlasov-Ampere system, which is the focus of this paper. The Vlasov equation describes the evolution of the probability density function of particle species in phase space, while Ampere's equation govern the evolution of the electric field. Ampere's equation is driven by the moment of the particle distribution, and the characteristics of the Vlasov equation are self-consistently determined by the field. This results in a tightly coupled nonlinear system that is challenging to solve. The specificity of PIC methods lies in their mixed discretization: an Eulerian grid for the moments of the particle distribution and fields, combined with individual Lagrangian particles in continuous phase space.

Traditionally, and still in most applications, PIC implementations use an explicit time discretization of the Vlasov equation. Explicit time integration offers simplicity of implementation and low computational cost per iteration. However, explicit methods suffer from temporal stability constraints, requiring small time steps to resolve the fastest waves. They also face spatial stability constraints, with numerical instabilities like the finite grid instability [27, 24] occurring when the grid cell size is equal to or larger than the plasma's Debye length.

PIC methods also contend with a significant challenge: the statistical error arising from sampling the probability density function with a finite number of numerical particles. This numerical noise decreases only slowly with an increase in the average number of particles per cell, scaling inversely with the square root of the mean number of particles per cell. The computational costs and storage requirements grow exponentially with the dimensionality of the problem, an issue known as the curse of dimensionality.

Thus, applying explicit PIC methods to multidimensional problems, especially three-dimensional geometries or high plasma densities, can be computationally demanding and cumbersome. In this paper, we address these computational challenges by proposing a numerical method that (i) alleviates the numerical constraints of explicit methods, maintaining

*Corresponding author
LIP6, Sorbonne Université, Paris, France

stability with larger time steps and grid sizes, and (ii) significantly mitigates the statistical error and reduces the size of the problem, offering gains in memory consumption and computational time.

To address the numerical stability challenges, implicit PIC schemes have been developed [14], gaining attention for their stability properties. Notable examples include the implicit-moment method [4, 30] and the direct implicit method [28, 6, 23]. These implicit methods alleviate numerical constraints, maintaining stability with larger time steps and grid sizes. Ideally, implicit methods should non-linearly couple the particle and field equations, requiring Newton or Picard iterations. However, due to early solver efficiency limitations, linear approximations were favored, leading to numerical approximations that violated energy conservation and caused significant artificial plasma heating or cooling. These methods, which linearize the particle-field coupling, are known as semi-implicit methods.

The solutions of the continuous Vlasov-Maxwell equations adhere to certain conservation properties, such as the conservation of total energy and momentum. The charge continuity equation also follows from the Vlasov equations (zero-order moment). The issue of conserving these physical quantities in numerical simulations has been a topic of interest for many years [3]. Explicit PIC methods typically conserve momentum but not energy. Conversely, implicit PIC implementations can conserve energy but not momentum.

Recently, a semi-implicit method known as the Energy-Conserving Semi-Implicit Method (ECSIM) was developed to exactly conserve the system's discrete total energy [29]. ECSIM retains the simplicity of explicit schemes, where particles are advanced first, followed by fields without iteration. By partially linearizing the particle-field coupling and using a mass matrix, ECSIM ensures exact discrete energy conservation. Unlike previous semi-implicit methods, ECSIM's particle pusher and field equation derivation are distinct, requiring no inner iteration and maintaining a complexity similar to explicit formulations. However, the field matrix is considerably more intricate to achieve energy conservation down to round-off errors. The primary advantage over fully implicit schemes is the reduced algorithmic complexity, facilitating development for three-dimensional simulations. This method has been extensively applied to large-scale kinetic simulations [35, 34, 5, 7].

Sparse grid reconstructions aim to mitigate the statistical error in PIC methods. These methods employ the sparse grid combination technique, wherein particle distribution moments are computed on a hierarchy of coarse resolution component grids. On each component grid, the average number of particles per cell is larger compared to standard grids, thereby reducing statistical noise or decreasing the total number of numerical particles needed for comparable precision. This approach has been applied to explicit PIC discretizations of the Vlasov-Poisson model in two dimensions [13] and three dimensions [33, 31, 10, 11], with extensions to high-order basis functions proposed [12]. It has been employed in classical benchmarks of kinetic plasma physics, such as the simulation of Landau damping and diocotron instability, and has been extended to the simulations of low-temperature (and collisional) plasma discharge, as well as drift instabilities in Hall plasma thrusters [16, 17, 19, 20]. Significant gains in memory consumption and computational time, by two to three orders of magnitude compared to standard grid approaches, have been documented.

The application of sparse grids to semi-implicit PIC methods was initially explored in [21]. This exploration led to the development of two schemes: the SISPIC-sg scheme and the ECSPIC[1] scheme. These schemes, akin to the ECSIM scheme in linearizing particle equations, adopt a div-Ampere formulation tailored for electrostatic regimes, ensuring the electromagnetic field is free from any solenoidal (or inductive) components. In the SISPIC-sg

[1]This scheme will be referred to as ECSPIC-1 in this paper, distinguishing it from the newly introduced scheme, which will be referred to as ECSPIC-2.

scheme, the explicit component of current density—acting as the source term of the Ampere equation—is computed using the sparse grid combination technique. Meanwhile, the implicit contribution is conventionally handled with standard grid techniques. The combination technique approximates current density on a hierarchy of coarse grids (component grids) and reconstructs a fine approximation through a linear combination of these coarse contributions. However, this approach does not conserve discrete total energy. Contrarily, the ECSPIC-1 scheme expands upon this approach by employing a comprehensive sparse grid discretization. It computes both components of current density across the hierarchy of component grids and discretizes the div-Ampere equation accordingly. To ensure exact conservation of discrete total energy, the electric field is interpolated at particle positions using the combination technique. Nonetheless, this scheme has exhibited numerical instability, attributed to the loss of non-negativity in the field energy, which is a combination of field energies defined on coarse grids. Designing a sparse grid scheme that exactly conserves total energy, defined as the sum of non-negative kinetic and field energies, poses a significant challenge due to the inherent property of the combination technique, which does not preserve non-negativity.

In this paper, we build upon the findings of [21] by introducing a novel semi-implicit PIC scheme based on sparse grid discretization that conserves exactly the discrete total energy while maintaining numerical stability. Named the ECSPIC-2 scheme, our method utilizes a Galerkin approach to the variational formulation of the div-Ampere equation. The source term, specifically the divergence of the current density, is computed using a density estimation technique [22, 32]. This technique seeks the optimal approximation within a finite-dimensional space, approximating the quantity as a sum of Dirac masses centered at particle positions. The finite-dimensional space used for both the Galerkin method of the div-Ampere equation and the density estimation is constructed from a hierarchical sparse grid representation of linear basis functions. To our knowledge, this method is the first sparse-PIC approach that does not rely on the combination technique. The sparse grid hierarchical representation employed here facilitates the definition of a non-negative field energy, thereby ensuring exact conservation of total energy encompassing non-negative kinetic and field energies, thereby maintaining stability. Indeed, throughout simulations, particle velocities and electric fields remain bounded, constrained by the initial total energy of the system. Additionally, our scheme benefits from computational cost reductions offered by sparse grid techniques. The size of the linear system to solve is reduced to $O\left(n^{d-1}2^n\right)$ compared to $O\left(2^{dn}\right)$ for standard ECSIM schemes or the SISPIC-sg scheme, where d represents the dimension of the problem and n is a spatial discretization parameter. Furthermore, statistical noise is reduced compared to standard schemes due to sparse grid discretization employing fewer and larger cells than standard discretizations, thereby ensuring more particles per cell in the simulation.

Key properties of the ECSPIC-2 scheme include:

- P_1: The scheme is consistent with an electrostatic formulation, *i.e.* it computes an irrotational electric field.
- P_2: The scheme is unconditionally stable with respect to the plasma period, allowing arbitrary time step choices.
- P_3: The finite grid instability is eliminated, allowing grid discretization without constraints related to the Debye length.
- P_4: The discrete total energy of the system is exactly conserved for any discretization parameters.
- P_5: The scheme is devoid of numerical instabilities associated with the loss of non-negativity of field energy.
- P_6: The statistical error is significantly reduced compared to standard schemes with grid of comparable resolution and the same number of particles.
- P_7: The size of the linear system is reduced compared to standard schemes with grid of

comparable resolution.

Table 1: Properties P_1-P_7 of the newly introduced scheme (ECSPIC-2) and the existing schemes (SISPIC-std, SISPIC-sg, ECSPIC , ECSIM).

scheme	reference	P_1	P_2	P_3	P_4	P_5	P_6	P_7
ECSIM	[29]	×	✓	✓	✓	✓	×	×
SISPIC-std	[21]	✓	✓	✓	✓	✓	×	×
SISPIC-sg	[21]	✓	✓	✓	×	✓	✓	×
ECSPIC-1	[21]	✓	✓	✓	✓	×	✓	✓
ECSPIC-2	this paper	✓	✓	✓	✓	✓	✓	✓

We provide Table 1 summarizing the properties P_1 to P_7 verified, or not, by existing semi-implicit methods and the ECSPIC-2 scheme.

This paper is organized as follows: Section 2 introduces the general framework of the article, focusing on the electrostatic Vlasov-(div)Ampere formulation and PIC methods. Section 3 focuses on the time discretization through a semi-implicit formulation and the spatial discretization employing Galerkin methods with sparse grids. Herein, the ECSPIC-2 scheme is introduced, emphasizing its properties including energy conservation, preservation of non-negativity, and the well-posedness of the linear system. Finally, Section 4 investigates and compares the method with existing approaches (explicit schemes, SISPIC-sg, ECSPIC) using two-dimensional classical test cases: Landau damping and two-streams instability.

2. General framework.

2.1. Notations. In this section, we establish the general framework and introduce the notations used throughout this paper. Let $d \in \mathbb{N}^*$ be the dimension of the problem, and let the spatial domain be the d-dimensional periodic unit interval $\Omega = (\mathbb{R}/\mathbb{Z})^d$. For multi-indices $\boldsymbol{\alpha} = (\alpha_1, \dots, \alpha_d) \in \mathbb{N}^d$ and $\boldsymbol{\beta} = (\beta_1, \dots, \beta_d) \in \mathbb{N}^d$, we define the following order relations:

$$\boldsymbol{\alpha} \leq \boldsymbol{\beta} \iff \forall i \in \{1, \dots, d\},\ \alpha_i \leq \beta_i, \tag{2.1}$$

$$\boldsymbol{\alpha} < \boldsymbol{\beta} \iff \boldsymbol{\alpha} \leq \boldsymbol{\beta} \text{ and } \exists\, i \in \{1, \dots, d\} \text{ such that } \alpha_i < \beta_i. \tag{2.2}$$

We also introduce the following notations:

$$\boldsymbol{\alpha}\boldsymbol{\beta} = (\alpha_1\beta_1, \dots, \alpha_d\beta_d), \qquad \boldsymbol{\alpha}^{-1} = \frac{1}{\alpha_1 \cdots \alpha_d}. \tag{2.3}$$

The l^1 and l^∞ norms for a multi-index $\boldsymbol{\alpha} \in \mathbb{N}^d$ are defined by:

$$|\boldsymbol{\alpha}|_1 := \sum_{i=1}^{d} |\alpha_i|, \quad |\boldsymbol{\alpha}|_\infty := \max_{i=1,\dots,d} |\alpha_i|. \tag{2.4}$$

2.2. Electrostatic Vlasov-div-Ampere (VdA) formulation. In this section, we recall the electrostatic VdA formulation introduced in [21], which defines the fundamental equations underpinning the scheme presented in this paper.

Definition 2.1 (Vlasov-div-Ampere (VdA) formulation). *In an electrostatic regime, i.e., with a vanishing magnetic field $\boldsymbol{B} = 0$, assuming initial potential $\Phi_0(\boldsymbol{x})$ and particle distri-*

bution $f_{s,0}(\boldsymbol{x}, \boldsymbol{v})$, the VdA formulation is given by:

$$(VdA): \begin{cases} \dfrac{\partial f_s}{\partial t}(\boldsymbol{x}, \boldsymbol{v}, t) + \boldsymbol{v} \cdot \boldsymbol{\nabla}_{\boldsymbol{x}} f_s(\boldsymbol{x}, \boldsymbol{v}, t) + \dfrac{q_s}{m_s} \boldsymbol{E}(\boldsymbol{x}, t) \cdot \boldsymbol{\nabla}_{\boldsymbol{v}} f_s(\boldsymbol{x}, \boldsymbol{v}, t) = 0, \\ \epsilon_0 \dfrac{\partial \Delta \Phi}{\partial t}(\boldsymbol{x}, t) = \boldsymbol{\nabla} \cdot \boldsymbol{J}(\boldsymbol{x}, t), \quad \boldsymbol{E}(\boldsymbol{x}, t) = -\boldsymbol{\nabla} \Phi(\boldsymbol{x}, t), \\ \Phi(\boldsymbol{x}, 0) = \Phi_0(\boldsymbol{x}), \quad f_s(\boldsymbol{x}, \boldsymbol{v}, 0) = f_{s,0}(\boldsymbol{x}, \boldsymbol{v}) \end{cases} \tag{2.5}$$

The system is defined for $(\boldsymbol{x}, \boldsymbol{v}, t) \in \Omega \times \mathbb{R}^d \times \mathbb{R}^+$. Here, $f_s(\boldsymbol{x}, \boldsymbol{v}, t)$ is the phase-space distribution function for species s; q_s and m_s are the corresponding charge and mass; ϵ_0 is the vacuum permittivity; Φ is the electric potential; $\boldsymbol{E}$ is the electric field; and $\boldsymbol{J}$ is the plasma current density derived from the phase-space distribution of each species:

$$\boldsymbol{J}(\boldsymbol{x}, t) = \sum_s \boldsymbol{J}_s(\boldsymbol{x}, t) = \sum_s q_s \int_{\mathbb{R}^d} \boldsymbol{v} f_s(\boldsymbol{x}, \boldsymbol{v}, t) d\boldsymbol{v}. \tag{2.6}$$

The initial electric potential is computed via the resolution of a Poisson equation:

$$-\varepsilon_0 \Delta \Phi_0(\boldsymbol{x}) = \rho_0(\boldsymbol{x}), \tag{2.7}$$

where $\rho_0(\boldsymbol{x})$ is the initial plasma charge density, defined from the initial distribution of each species:

$$\rho_0(\boldsymbol{x}) = \sum_s \rho_{s,0}(\boldsymbol{x}) = \sum_s q_s n_s, \quad n_s = \int_{\mathbb{R}^d} f_{s,0}(\boldsymbol{x}, \boldsymbol{v}) d\boldsymbol{v}. \tag{2.8}$$

The VdA system is equivalent to the Vlasov-Ampere (VA) system in electrostatic regimes:

$$(VA): \begin{cases} \dfrac{\partial f_s}{\partial t}(\boldsymbol{x}, \boldsymbol{v}, t) + \boldsymbol{v} \cdot \boldsymbol{\nabla}_{\boldsymbol{x}} f_s(\boldsymbol{x}, \boldsymbol{v}, t) + \dfrac{q_s}{m_s} \boldsymbol{E}(\boldsymbol{x}, t) \cdot \boldsymbol{\nabla}_{\boldsymbol{v}} f_s(\boldsymbol{x}, \boldsymbol{v}, t) = 0, \\ \boldsymbol{\nabla} \times \boldsymbol{E}(\boldsymbol{x}, t) = 0, \\ \epsilon_0 \dfrac{\partial \boldsymbol{E}}{\partial t}(\boldsymbol{x}, t) = -\boldsymbol{J}(\boldsymbol{x}, t), \end{cases} \tag{2.9}$$

Indeed, since the electric field is derived from a potential, its curl vanishes:

$$\boldsymbol{\nabla} \times \boldsymbol{E} = -\boldsymbol{\nabla} \times \boldsymbol{\nabla} \Phi = 0. \tag{2.10}$$

Traditionally, the VA system is commonly employed in implicit PIC methods. However, in electrostatic regimes and multidimensional settings, enforcing the irrotational electric field condition ($\boldsymbol{\nabla} \times \boldsymbol{E} = 0$) numerically poses challenges. Therefore, our scheme is derived from the VdA formulation, which is more suitable for electrostatic regimes.

Remark 2.2. *If the charge continuity equation or the Gauss's law, defined by:*

$$\frac{\partial \rho}{\partial t}(\boldsymbol{x}, t) + \boldsymbol{\nabla} \cdot \boldsymbol{J}(\boldsymbol{x}, t) = 0, \quad \boldsymbol{\nabla} \cdot \boldsymbol{E}(\boldsymbol{x}, t) = \frac{1}{\varepsilon_0} \rho(\boldsymbol{x}, t), \tag{2.11}$$

is satisfied, the VdA (and VA) formulation is equivalent to the electrostatic Vlasov-Poisson (VP) formulations, traditionally used in explicit schemes:

$$(VP): \begin{cases} \dfrac{\partial f_s}{\partial t}(\boldsymbol{x}, \boldsymbol{v}, t) + \boldsymbol{v} \cdot \boldsymbol{\nabla}_{\boldsymbol{x}} f_s(\boldsymbol{x}, \boldsymbol{v}, t) + \dfrac{q_s}{m_s} \boldsymbol{E}(\boldsymbol{x}, t) \cdot \boldsymbol{\nabla}_{\boldsymbol{v}} f_s(\boldsymbol{x}, \boldsymbol{v}, t) = 0, \\ -\epsilon_0 \Delta \Phi(\boldsymbol{x}, t) = \rho(\boldsymbol{x}, t), \quad \boldsymbol{E}(\boldsymbol{x}, t) = -\boldsymbol{\nabla} \Phi(\boldsymbol{x}, t). \end{cases} \tag{2.12}$$

2.3. Particle-In-Cell (PIC) discretizations. In PIC methods, the distribution of particles (f_s) is represented by a collection of macro-particles. A macro-particle, also called a numerical particle, refers to a group of physical particles of the same species (*e.g.*, electrons, ions). Let N_s denote the number of macro-particles associated with species s and N the total number of particles. The positions and velocities of a particle at time t are denoted by $(\boldsymbol{x}_p(t), \boldsymbol{v}_p(t))$, where $p = 1, ..., N_s$ is the index of the particles. We assume that all the numerical particles of one species have the same weight, defined by the ratio of physical particles (n_s) to numerical particles (N_s):

$$\omega_p = \frac{\int_\Omega n_s d\boldsymbol{x}}{N_s}, \quad \forall p = 1, ..., N_s \tag{2.13}$$

and the same charge and mass:

$$q_p = q_s \omega_p, \quad m_p = m_s \omega_p, \qquad \forall p = 1, ..., N_s. \tag{2.14}$$

The numerical distribution of the particles is defined by the sum of Dirac masses centered at particle positions and velocities:

$$f_{s,N}(\boldsymbol{x}, \boldsymbol{v}, t) = \sum_{p=1}^{N_s} \omega_p \delta(\boldsymbol{x} - \boldsymbol{x}_p(t)) \delta(\boldsymbol{v} - \boldsymbol{v}_p(t)). \tag{2.15}$$

Positions and velocities are initialized such that $f_{s,N}(\boldsymbol{x}, \boldsymbol{v}, 0)$ is a good approximation of the initial distribution function $f_{s,0}(\boldsymbol{x}, \boldsymbol{v})$. From this approximation, the moments of the particle distribution, i.e. the current and charge densities, can be defined by:

$$\boldsymbol{J}_N(\boldsymbol{x}, t) = \sum_s q_s \int_{\mathbb{R}^d} f_{s,N}(\boldsymbol{x}, \boldsymbol{v}, t) \boldsymbol{v} d\boldsymbol{v}, \quad \rho_N(\boldsymbol{x}, t) = \sum_s q_s \int_{\mathbb{R}^d} f_{s,N}(\boldsymbol{x}, \boldsymbol{v}, t) d\boldsymbol{v}. \tag{2.16}$$

Specifically, it leads the following definition of the current density, which is of particular interest in this work:

Definition 2.3 (Numerical approximation of current density). *The current density, that is the source term of Ampere equation, is defined by:*

$$\boldsymbol{J}_N(\boldsymbol{x}, t) = \sum_s \sum_{p=1}^{N_s} q_p \boldsymbol{v}_p(t) \delta(\boldsymbol{x} - \boldsymbol{x}_p(t)). \tag{2.17}$$

In PIC methods, the moments of the particle distribution must be approximated on a mesh to solve the field equations using mesh-based techniques (*e.g.*, finite element or finite difference methods). Typically, a shape function W_h, dependent on the mesh discretization parameter h, is associated with the particles to perform the density accumulation onto the mesh. In this article, we instead consider a density estimation technique [22, 32] to compute an approximation of these quantities on the mesh. The idea is to seek the best approximation of $\boldsymbol{J}_N$, or ρ_N, in a suitable finite-dimensional space. This procedure will be defined later in the paper.

An approximation of the electric field is computed using the fields equations and interpolated at the particle positions. Finally, the particles are advanced by considering the characteristics of the Vlasov equation:

$$\begin{cases} \dfrac{d\boldsymbol{x}_p(t)}{dt} & = \boldsymbol{v}_p(t), \\ \dfrac{d\boldsymbol{v}_p(t)}{dt} & = \frac{q_s}{m_s} \boldsymbol{E}(\boldsymbol{x}_p(t), t), \\ \boldsymbol{x}_p(0) & = \boldsymbol{x}_p^0, \quad \boldsymbol{v}_p(0) = \boldsymbol{v}_p^0. \end{cases} \tag{2.18}$$

3. Energy-conserving method using sparse grid.

3.1. Spatial and time discretizations.

3.1.1. Implicit formulation and linearization. Let $\Delta t \in \mathbb{R}_+^*$ denote the time discretization step, and let the superscript $k \in \mathbb{N}$ represents the evaluation of quantities at iteration k:

$$t^k := k\Delta t, \quad \boldsymbol{x}_p^k := \boldsymbol{x}_p(t^k), \quad \boldsymbol{v}_p^k := \boldsymbol{v}_p(t^k), \text{ etc.} \tag{3.1}$$

We introduce our implicit scheme used for the time discretization of the electrostatic VdA system of Eq. (2.5), where the position is staggered half a time step with respect to the velocities and the fields as follows:

$$\begin{cases} \boldsymbol{x}_p^{k+\frac{1}{2}} = \boldsymbol{x}_p^{k-\frac{1}{2}} + \Delta t \boldsymbol{v}_p^{k+\frac{1}{2}} \\ \boldsymbol{v}_p^{k+1} = \boldsymbol{v}_p^k + \Delta t \dfrac{q_p}{m_p} \boldsymbol{E}^{k+\frac{1}{2}}\left(\boldsymbol{x}_p^{k+\frac{1}{2}}\right) \\ \Delta\Phi^{k+1} - \Delta\Phi^k = \dfrac{\Delta t}{\varepsilon_0} \boldsymbol{\nabla} \cdot \boldsymbol{J}^{k+\frac{1}{2}} \\ \boldsymbol{E}^{k+1} = -\boldsymbol{\nabla}\Phi^{k+1} \end{cases}, \quad k \in \mathbb{N}. \tag{3.2}$$

The following averaged quantities have been introduced:

$$\boldsymbol{v}_p^{k+\frac{1}{2}} = \frac{1}{2}\left(\boldsymbol{v}_p^{k+1} + \boldsymbol{v}_p^k\right), \quad \boldsymbol{E}^{k+\frac{1}{2}}\left(\boldsymbol{x}_p^{k+\frac{1}{2}}\right) := \frac{1}{2}\left[\boldsymbol{E}^{k+1}\left(\boldsymbol{x}_p^{k+\frac{1}{2}}\right) + \boldsymbol{E}^k\left(\boldsymbol{x}_p^{k+\frac{1}{2}}\right)\right]. \tag{3.3}$$

The scheme introduced in Eq. (3.2) is fully implicit due to the coupling between particles and fields. It requires solving a nonlinear system. Semi-implicit approaches, such as the moment implicit method [4, 30], the direct implicit method [28, 23], or the method introduced here, are based on a linearization of the equations. However, the method introduced in this paper differs from the direct implicit method (where the shape function W_h is linearized using Taylor expansions) and the moment implicit method (where the linearization is obtained from moments of the Vlasov equation). The method is similar to the one introduced in [21], inspired by the ECSIM method [29]. The linearization is obtained directly in the particle equations by updating the particle positions with a known velocity, i.e., the first equation in Eq. (3.2) becomes:

$$\boldsymbol{x}_p^{k+\frac{1}{2}} = \boldsymbol{x}_p^{k-\frac{1}{2}} + \frac{\Delta t}{2}\left[\boldsymbol{v}_p^k + \Delta t \frac{q_p}{m_p} \boldsymbol{E}^{k+\frac{1}{2}}\left(\boldsymbol{x}_p^{k+\frac{1}{2}}\right) + \boldsymbol{v}_p^k\right] \tag{3.4}$$

$$= \boldsymbol{x}_p^k + \Delta t \boldsymbol{v}_p^k + O\left(\Delta t^2\right). \tag{3.5}$$

As a result, the implicit model becomes linear so that the implicit contribution of the electric field (evaluated at the known particle position) can be obtained from the div-Ampere equation by solving a linear system. The particle equations then are:

Definition 3.1 (Particle equations). *Given the electric field at time step k and $k+1$, the particles are advanced according to:*

$$\begin{cases} \boldsymbol{x}_p^{k+\frac{1}{2}} = \boldsymbol{x}_p^{k-\frac{1}{2}} + \Delta t \boldsymbol{v}_p^k, \\ \boldsymbol{v}_p^{k+1} = \boldsymbol{v}_p^k + \Delta t \dfrac{q_p}{m_p} \boldsymbol{E}^{k+\frac{1}{2}}\left(\boldsymbol{x}_p^{k+\frac{1}{2}}\right) \end{cases}, \quad k \in \mathbb{N}. \tag{3.6}$$

3.1.2. Spatial discretization with Galerkin methods. We proceed with the spatial discretization of the field equations (div-Ampere and electric field) using a Galerkin method applied to their variational formulations. Let $V := H^1(\Omega)$ denote the Sobolev space H^1, comprising functions with integrable weak derivatives in the L^2 norm. The variational form of the div-Ampere equation in this space is expressed as:

$$\int_\Omega (\Delta\Phi^{k+1} - \Delta\Phi^k) v d\boldsymbol{x} = \frac{\Delta t}{\varepsilon_0} \int_\Omega \mathcal{J}^{k+\frac{1}{2}} v d\boldsymbol{x}, \quad \forall v \in V, \tag{3.7}$$

where $\mathcal{J}^{k+\frac{1}{2}} := \boldsymbol{\nabla} \cdot \boldsymbol{J}^{k+\frac{1}{2}}$ is a shortcut notation for the divergence of the current density. Applying an integration by parts on the periodic domain Ω, one gets:

$$-\int_\Omega (\boldsymbol{\nabla}\Phi^{k+1} - \boldsymbol{\nabla}\Phi^k) \cdot \boldsymbol{\nabla} v d\boldsymbol{x} = \frac{\Delta t}{\varepsilon_0} \int_\Omega \mathcal{J}^{k+\frac{1}{2}} v d\boldsymbol{x}, \quad \forall v \in V. \tag{3.8}$$

Similarly, the variational form of the relation between the electric field and the potential is given by:

$$\int_\Omega \boldsymbol{E}^{k+1} v d\boldsymbol{x} = -\int_\Omega \boldsymbol{\nabla}\Phi^{k+1} v d\boldsymbol{x}, \quad \forall v \in V. \tag{3.9}$$

Let us now detail the procedure to approximate the divergence of the current density, *i.e.* the source term of the div-Ampere (see Eq. (3.7)). It is based on nonparametric density estimation techniques with splines smoothing [22, 32]. The task is to construct an estimated density function based on a data set of samples drawn from an unknown distribution with unknown probability density function. The idea is to first give us a highly-overfitted guess of the density of interest and then use spline smoothing to obtain a better approximation. In our case we seek an approximation of $\mathcal{J}^{k+1/2}$ by considering the set of the particle positions as data samples. We choose the numerical approximation of the current density by Dirac masses, defined by Eq. (2.17), as the highly-overfitted guess:

$$\tilde{\mathcal{J}}_N^{k+\frac{1}{2}} = \boldsymbol{\nabla} \cdot \boldsymbol{J}_N^{k+\frac{1}{2}}. \tag{3.10}$$

The idea of spline smoothing is to consider the following minimization problem:

$$\mathcal{J}^{k+\frac{1}{2}} := \underset{\tilde{\mathcal{J}} \in V}{\operatorname{argmin}} \int_\Omega \left(\tilde{\mathcal{J}} - \tilde{\mathcal{J}}_N^{k+\frac{1}{2}} \right)^2 d\boldsymbol{x}. \tag{3.11}$$

Here we seek the optimal approximation in L^2-norm of our highly-overfitted guess in the space V. Usually the space V is substituted by a finite dimensional space of spline functions. The minimization problem can be reformulated in weak form as:

$$\int_\Omega \mathcal{J}^{k+\frac{1}{2}} v d\boldsymbol{x} = \int_\Omega \tilde{\mathcal{J}}_N^{k+\frac{1}{2}} v d\boldsymbol{x}, \quad \forall v \in V. \tag{3.12}$$

Note here that our highly-overfitted guess is only well-defined if considered within an integral as in Eq. (3.12).

Remark 3.2. *The approach introduced here to approximate the divergence of the current density is different from the one used in the SISPIC and ECSPIC schemes [21]. In that previous work, a shape function W_h/h^d, that is continuous, linear by part and with support scaled on the mesh discretization h, is introduced to compute an approximation of the current*

density. By identifying $\boldsymbol{J}_N^{k+1/2}$ as a Radon measure, an approximation is defined on the mesh by:

(3.13)
$$\boldsymbol{J}_{h,N}^{k+\frac{1}{2}}(\boldsymbol{x}_j) := \langle \boldsymbol{J}_N^{k+\frac{1}{2}}, \frac{W_h}{h^d}(\boldsymbol{x}_j - \cdot)\rangle = \sum_s \sum_{p=1}^{N_s} q_p \boldsymbol{v}_p^{k+\frac{1}{2}} \frac{W_h}{h^d}(\boldsymbol{x}_j - \boldsymbol{x}_p(t)), \quad \forall j = 1, ..., N_h,$$

where N_h is the number of grid nodes. The divergence of the current density is then defined by applying a discrete divergence operator $\boldsymbol{\nabla}_h$ to this quantity. Note that this approach introducing a shape function is also used in all existing explicit sparse-PIC schemes, computing an approximation of the charge density.

By substituting Eq. (3.12) to Eq. (3.8) and performing integration by parts on the right side, one gets:

$$\int_\Omega (\boldsymbol{\nabla}\Phi^{k+1} - \boldsymbol{\nabla}\Phi^k) \cdot \boldsymbol{\nabla} v d\boldsymbol{x} = \frac{\Delta t}{\varepsilon_0} \int_\Omega \boldsymbol{J}_N^{k+\frac{1}{2}} \cdot \boldsymbol{\nabla} v d\boldsymbol{x}, \quad \forall v \in V, \tag{3.14}$$

We proceed with a Galerkin method by introducing a finite-dimensional approximation space $V_h \subset V$, defined as:

$$V_h := \text{span}\{W_{h,1}, \ldots, W_{h,N_h}\}, \tag{3.15}$$

where N_h is the dimension of V_h, representing the number of basis functions employed. The specific construction of V_h will be detailed in the subsequent section. By expanding the electric potential in terms of the basis functions of V_h, we derive the discretized div-Ampere equation:

Definition 3.3 (Discretized div-Ampere equation). *The Galerkin method of the div-Ampere equation with respect to the approximation space V_h is formulated as:*

$$\sum_{j=1}^{N_h} (\hat{\Phi}_j^{k+1} - \hat{\Phi}_j^k) \int_\Omega \boldsymbol{\nabla} W_{h,i} \cdot \boldsymbol{\nabla} W_{h,j} d\boldsymbol{x} = \frac{\Delta t}{\varepsilon_0} \sum_s \sum_{p=1}^{N_s} q_p \boldsymbol{v}_p^{k+\frac{1}{2}} \cdot \left(\int_\Omega \delta\left(\boldsymbol{x} - \boldsymbol{x}_p^{k+\frac{1}{2}}\right) \boldsymbol{\nabla} W_{h,i} d\boldsymbol{x} \right), \quad \forall i = 1, ..., N_h. \tag{3.16}$$

where hatted quantities denote coefficients in the basis of V_h.

Let $\boldsymbol{E}_h^{k+\frac{1}{2}}$ be the approximation of the electric field in V_h. Upon solving equation (3.16), we define the electric field interpolated at the particle positions through convolution with a Dirac delta function centered at these positions:

$$\boldsymbol{E}_{h,N}^{k+\frac{1}{2}}\left(\boldsymbol{x}_p^{k+\frac{1}{2}}\right) := \int_\Omega \delta\left(\boldsymbol{x} - \boldsymbol{x}_p^{k+\frac{1}{2}}\right) \boldsymbol{E}_h^{k+\frac{1}{2}} d\boldsymbol{x}. \tag{3.17}$$

By utilizing (3.9) and performing integrations by parts, we obtain the following representation of the electric field.

Definition 3.4 (Interpolation of the electric field). *Let $\hat{\Phi}_j^{k+1}, \hat{\Phi}_j^k$ be the coefficients of the electric potential in the basis of V_h, computed by Eq. (3.16), then the electric field interpolated at particle positions is expressed as:*

$$\boldsymbol{E}_{h,N}^{k+\frac{1}{2}}\left(\boldsymbol{x}_p^{k+\frac{1}{2}}\right) = -\sum_{j=1}^{N_h} \hat{\Phi}_j^{k+\frac{1}{2}} \int_\Omega \delta\left(\boldsymbol{x} - \boldsymbol{x}_p^{k+\frac{1}{2}}\right) \boldsymbol{\nabla} W_{h,j} d\boldsymbol{x}, \tag{3.18}$$

where $\hat{\Phi}_j^{k+\frac{1}{2}} = (\hat{\Phi}_j^{k+1} + \hat{\Phi}_j^k)/2$.

3.1.3. Hierarchical sparse grid discretizations. We introduce some background on the sparse grids. Let $\boldsymbol{l} \in \mathbb{N}^d$, $\boldsymbol{j} \in \mathbb{N}^d$ be multi-indexes and $h_{\boldsymbol{l}} = (2^{-l_1}, ..., 2^{-l_d}) \in \mathbb{R}^d$ be the sparse grid discretization. Let us consider basis functions defined by tensor products of one-dimensional hat functions as follows:

(3.19)
$$W_{h_{\boldsymbol{l}},\boldsymbol{j}}(\boldsymbol{x}) := \left(\bigotimes_{i=1}^{d} W_{h_{l_i},j_i}\right)(\boldsymbol{x}), \quad W_{h_{l_j},j_i}(x) := W\left(h_{l_i}^{-1}(x_i - j_i h_{l_i})\right), \quad W(x) = \max\left(1 - |x|, 0\right).$$

A space of d-dimensional hat functions, denoted $V_{h_{\boldsymbol{l}}}$, is defined by:

$$V_{h_{\boldsymbol{l}}} := \text{span}\{W_{h_{\boldsymbol{l}},\boldsymbol{j}} \mid \boldsymbol{j} \in I_{h_{\boldsymbol{l}}}\}, \quad I_{h_{\boldsymbol{l}}} := [\![0, h_{l_1}^{-1} - 1]\!] \times ... \times [\![0, h_{l_d}^{-1} - 1]\!] \subset \mathbb{N}^d \tag{3.20}$$

where $\{W_{h_{\boldsymbol{l}},\boldsymbol{j}} \mid \boldsymbol{j} \in I_{h_{\boldsymbol{l}}}\}$ is called the nodal basis of the space $V_{h_{\boldsymbol{l}}}$ and $I_{h_{\boldsymbol{l}}}$ the nodal basis index set. The basis functions verify a partition of unity property:

$$\sum_{\boldsymbol{j} \in I_{h_{\boldsymbol{l}}}} W_{h_{\boldsymbol{l}},\boldsymbol{j}}(\boldsymbol{x}) = 1. \tag{3.21}$$

Additionally, we introduce hierarchical increments of $V_{h_{\boldsymbol{l}}}$, denoted by $U_{h_{\boldsymbol{l}}}$ and defined by:

$$U_{h_{\boldsymbol{l}}} := V_{h_{\boldsymbol{l}}} \backslash \bigoplus_{i=1}^{d} V_{h_{\boldsymbol{l}-\boldsymbol{e}_i}}, \quad \text{where } V_{h_{\boldsymbol{l}}} := 0 \ \text{ if } \exists i \in \{1, ..., d\} \ s.t. \ l_i = -1, \tag{3.22}$$

and $\boldsymbol{e}_i \in \mathbb{N}^d$ is the unit vector with the i^{th} coordinate equal to one. The hierarchical increment comprises all $W_{h_{\boldsymbol{l}},\boldsymbol{j}} \in V_{h_{\boldsymbol{l}}}$ not included in smaller $V_{h_{\boldsymbol{k}}}$, with $\boldsymbol{k} < \boldsymbol{l}$, and can also be expressed as:

$$U_{h_{\boldsymbol{l}}} = \text{span}\{W_{h_{\boldsymbol{l}},\boldsymbol{j}} \mid \boldsymbol{j} \in \mathcal{B}_{h_{\boldsymbol{l}}}\}, \quad \mathcal{B}_{h_{\boldsymbol{l}}} := \left\{\boldsymbol{j} \in \mathbb{N}^d \mid \boldsymbol{0} \leq \boldsymbol{j} \leq h_{\boldsymbol{l}}^{-1}, \ \boldsymbol{j} \text{ odd}\right\}, \tag{3.23}$$

where $\{W_{h_{\boldsymbol{l}},\boldsymbol{j}} \mid \boldsymbol{j} \in \mathcal{B}_{h_{\boldsymbol{l}}}\}$ is called the hierarchical basis of the space $V_{h_{\boldsymbol{l}}}$ and $\mathcal{B}_{h_{\boldsymbol{l}}}$ the hierarchical basis index set. The space of piecewise d-linear functions of level $\boldsymbol{l}$ can be represented with its hierarchical basis:

$$V_{h_{\boldsymbol{l}}} = \bigoplus_{k_1 \leq l_1} ... \bigoplus_{k_d \leq l_d} U_{h_{\boldsymbol{k}}} = \bigoplus_{\boldsymbol{k} \leq \boldsymbol{l}} U_{h_{\boldsymbol{k}}}, \tag{3.24}$$

Thus, each function $v_{h_{\boldsymbol{l}}} \in V_{h_{\boldsymbol{l}}}$ can be represented in the hierarchical or nodal basis of $V_{h_{\boldsymbol{l}}}$:

$$v_{h_{\boldsymbol{l}}} = \sum_{\boldsymbol{k} \leq \boldsymbol{l}} \sum_{\boldsymbol{j} \in \mathcal{B}_{h_{\boldsymbol{k}}}} \hat{v}_{\boldsymbol{k},\boldsymbol{j}} W_{h_{\boldsymbol{k}};\boldsymbol{j}}, \quad v_{h_{\boldsymbol{l}}} = \sum_{\boldsymbol{j} \in I_{h_{\boldsymbol{l}}}} v_{\boldsymbol{l},\boldsymbol{j}} W_{h_{\boldsymbol{l}},\boldsymbol{j}}, \tag{3.25}$$

where $\hat{v}_{\boldsymbol{k},\boldsymbol{j}}$ are the coefficients of $v_{h_{\boldsymbol{l}}}$ in the hierarchical basis, called hierarchical surplus, and $v_{\boldsymbol{l},\boldsymbol{j}}$ are the coefficients of $v_{h_{\boldsymbol{l}}}$ in the nodal basis which are the nodal values of the function $v_{h_{\boldsymbol{l}}}$. The hierarchical surplus are defined by the application of a d-dimensional stencil as follows:

(3.26)
$$\hat{v}_{\boldsymbol{k},\boldsymbol{j}} := \mathscr{H}_{\boldsymbol{k},\boldsymbol{j}} v, \quad \mathscr{H}_{\boldsymbol{k},\boldsymbol{j}} = \bigotimes_{i=1}^{d} \mathscr{H}_{k_i,j_i}, \quad \mathscr{H}_{k_i,j_i} v = v(j_i h_{l_i}) + \frac{1}{2}\left[v\left(\frac{j_i - 1}{2} h_{l_i}\right) + v\left(\frac{j_i + 1}{2} h_{l_i}\right)\right].$$

We introduce a discrete approximation space, of dimension denoted by N_{h_n}, which is the space of d-dimensional piecewise linear functions with respect to the set of indices $\mathbb{L}$ and is denoted $V_{h_n}^{\mathbb{L}}$:

$$V_{h_n}^{\mathbb{L}} = \bigoplus_{\boldsymbol{l}\in\mathbb{L}} U_{h_{\boldsymbol{l}}}, \quad N_{h_n} := \left|V_{h_n}^{\mathbb{L}}\right|. \tag{3.27}$$

Here, $h_n = 2^{-n}$, $n \in \mathbb{N}^*$, denotes the underlying grid discretization and $\mathbb{L}$ is a multi-index set allowing to disqualify some of the subspaces in the approximation space. For example, $\mathbb{L}^{(\infty)} = \{\boldsymbol{l} \in \mathbb{N}^d \mid |\boldsymbol{l}|_\infty \leq n\}$ leads to the standard approximation space and $\mathbb{L}^{(1)} = \{\boldsymbol{l} \in \mathbb{N}^d \mid |\boldsymbol{l}|_1 \leq n\}$ leads to the traditional sparse grid approximation space. The dimension of the space depends on the choice of the multi-index $\mathbb{L}$, *e.g.*

$$\left|V_{h_n}^{\mathbb{L}^{(\infty)}}\right| = h_n^{-d}, \quad \left|V_{h_n}^{\mathbb{L}^{(1)}}\right| = h_n^{-1}\frac{n^{d-1}}{(d-1)!}. \tag{3.28}$$

Remark 3.5. *The hierarchical sparse grid representation adopted here for spatial discretization distinguishes itself from all existing sparse-PIC schemes (both explicit and semi-implicit). Traditionally, sparse-PIC methods discretize quantities of interest using nodal basis functions on a hierarchy of coarse grids known as component grids, which are then reconstructed via linear combinations:*

$$v_{h_n}^c = \sum_{i=0}^{d-1} \sum_{|\boldsymbol{l}|_1=n+d-1} \sum_{\boldsymbol{l}\geq 1} c_{\boldsymbol{l}} \sum_{\boldsymbol{j}\in I_{h_{\boldsymbol{l}}}} v_{\boldsymbol{l},\boldsymbol{j}} W_{h_{\boldsymbol{l}},\boldsymbol{j}}, \tag{3.29}$$

where $c_{\boldsymbol{l}}$ represents combination coefficients [13], typically taking values of 1 *or* -1 *in two dimensions. This technique, referred to as the combination technique, is illustrated in Fig.* 1 *and contrasted with the hierarchical sparse grid method.*

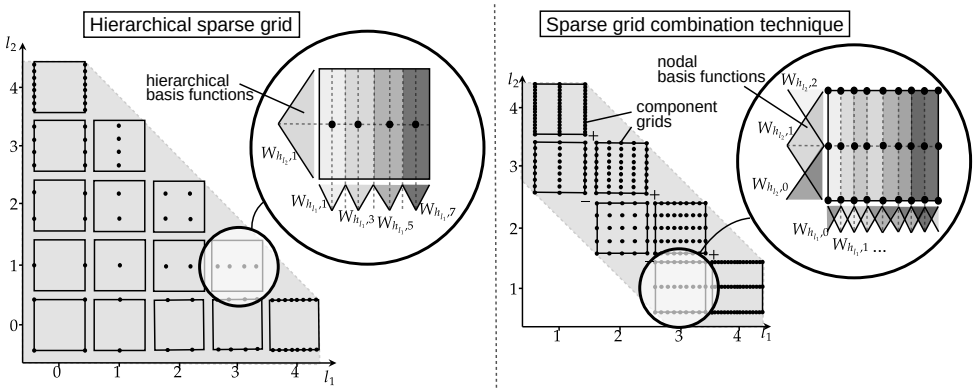

Fig. 1: Hierarchical sparse grid and combination technique discretizations for $n = 4$.

3.1.4. Derivation of the linear sytem. In this section, we introduce the algebraic manipulations leading to the linear system to solve. Building upon the Galerkin method of the div-Ampere equation outlined in previous sections, we apply it to the sparse grid approximation space defined in Eq. (3.27), with $\mathbb{L} = \mathbb{L}^{(1)}$. By employing Eq. (3.16) with the

basis functions from this space, the discretized div-Ampere equation's right-hand side can be decomposed into explicit and implicit components:

(3.30)
$$\sum_{\boldsymbol{l}\in\mathbb{L}^{(1)}}\sum_{\boldsymbol{j}\in\mathcal{B}_{h_l}}(\hat{\boldsymbol{\Phi}}_{\boldsymbol{l},\boldsymbol{j}}^{k+1}-\hat{\boldsymbol{\Phi}}_{\boldsymbol{l},\boldsymbol{j}}^{k})\int_\Omega \boldsymbol{\nabla}W_{h_l,\boldsymbol{i}}\cdot\boldsymbol{\nabla}W_{h_l,\boldsymbol{j}}d\boldsymbol{x}=\underbrace{\overset{k}{h}_{\bar{l},\boldsymbol{i}}}_{\text{explicit}}+\underbrace{\overset{k+1}{h}_{\bar{l},\boldsymbol{i}}}_{\text{implicit}},\quad\forall\bar{\boldsymbol{l}}\in\mathbb{L}^{(1)},\boldsymbol{i}\in\mathcal{B}_{h_{\bar{l}}}.$$

Here, the explicit and implicit components are defined as:

$$\overset{k}{h}_{\bar{l},\boldsymbol{i}}:=\sum_s\sum_{p=1}^{N_s}\frac{\Delta t q_p}{\varepsilon_0}\boldsymbol{v}_p^k\cdot\left(\int_\Omega\delta\left(\boldsymbol{x}-\boldsymbol{x}_p^{k+\frac{1}{2}}\right)\boldsymbol{\nabla}W_{h_{\bar{l}},\boldsymbol{i}}d\boldsymbol{x}\right),\tag{3.31}$$

$$\overset{k+1}{h}_{\bar{l},\boldsymbol{i}}:=\sum_s\sum_{p=1}^{N_s}\frac{q_p^2\Delta t^2}{2m_p\varepsilon_0}\boldsymbol{E}_{h,N}^{k+\frac{1}{2}}\left(\boldsymbol{x}_p^{k+\frac{1}{2}}\right)\cdot\left(\int_\Omega\delta\left(\boldsymbol{x}-\boldsymbol{x}_p^{k+\frac{1}{2}}\right)\boldsymbol{\nabla}W_{h_{\bar{l}},\boldsymbol{i}}d\boldsymbol{x}\right),\tag{3.32}$$

where we utilize the second equation of Eq. (3.6) and the subsequent relation:

$$\boldsymbol{v}_p^{k+\frac{1}{2}}=\boldsymbol{v}_p^k+\frac{(\boldsymbol{v}_p^{k+1}+\boldsymbol{v}_p^k)}{2}.\tag{3.33}$$

The electric field is interpolated at the particle positions according to the relation:

$$\boldsymbol{E}_{h_n,N}^{k+\frac{1}{2}}\left(\boldsymbol{x}_p^{k+\frac{1}{2}}\right)=-\sum_{\boldsymbol{l}\in\mathbb{L}^{(1)}}\sum_{\boldsymbol{j}\in\mathcal{B}_{h_l}}\frac{1}{2}\left(\hat{\boldsymbol{\Phi}}_{\boldsymbol{l},\boldsymbol{j}}^{k+1}+\hat{\boldsymbol{\Phi}}_{\boldsymbol{l},\boldsymbol{j}}^{k}\right)\int_\Omega\delta\left(\boldsymbol{x}-\boldsymbol{x}_p^{k+\frac{1}{2}}\right)\boldsymbol{\nabla}W_{h_l,\boldsymbol{j}}d\boldsymbol{x}.\tag{3.34}$$

Let us now define the following stiffness matrices:

$$\left(\mathbb{K}_{\boldsymbol{j},\boldsymbol{i}}^{h_l,h_{\bar{l}}}\right):=\int_\Omega\boldsymbol{\nabla}W_{h_l,\boldsymbol{j}}\cdot\boldsymbol{\nabla}W_{h_{\bar{l}},\boldsymbol{i}}d\boldsymbol{x},\tag{3.35}$$

$$\left(\mathbb{S}_{\boldsymbol{j},\boldsymbol{i}}^{h_l,h_{\bar{l}}}\right):=\sum_s\sum_{p=1}^{N_s}\frac{q_p^2\Delta t^2}{4m_p\varepsilon_0}\left(\int_\Omega\delta\left(\boldsymbol{x}-\boldsymbol{x}_p^{k+\frac{1}{2}}\right)\boldsymbol{\nabla}W_{h_l,\boldsymbol{j}}\cdot\boldsymbol{\nabla}W_{h_{\bar{l}},\boldsymbol{i}}d\boldsymbol{x}\right).\tag{3.36}$$

The first matrix represents the discretization of the Laplacian operator with Galerkin methods, whereas the second matrix denotes the linear term reflecting the particle response to the electric potential. It is noteworthy that the second stiffness matrix varies between iterations due to its dependence on particle positions, necessitating its computation at each step. In contrast, the first stiffness matrix remains unchanged and can be computed initially.

Let $\hat{\boldsymbol{\Phi}}^k$ denote the vector comprising all hierarchical coefficients of the potential at time k and $^{k,h_{\bar{l}}}$ the vector representing the explicit contribution of the current divergence. The contribution of the electric potential at time $k+1$ can thus be obtained by solving the following linear system:

$$\left(\mathbb{K}^{h_l,h_{\bar{l}}}+\mathbb{S}^{h_l,h_{\bar{l}}}\right)\hat{\boldsymbol{\Phi}}^{k+1}=\,^{k,h_{\bar{l}}}+\left(\mathbb{K}^{h_l,h_{\bar{l}}}-\mathbb{S}^{h_l,h_{\bar{l}}}\right)\hat{\boldsymbol{\Phi}}^{k}.\tag{3.37}$$

The main steps of the scheme are summarized in Algorithm 3.1.

Algorithm 3.1 Overview of ECSPIC-2 scheme.

Compute the stiffness matrix $\mathbb{K}^{h_l,h_{\bar{l}}}$.
Compute an initial approximation of the electric potential $\Phi^0_{h_n}$ by solving[1] Poisson equation, *i.e.* Eq. (2.7).
for each time step $k\Delta t$ **do**
Advance the particle positions in time with an explicit contribution of the particle velocity:

$$\mathbf{x}_p^{k+1/2} = \mathbf{x}_p^{k-1/2} + \Delta t \mathbf{v}_p^k.$$

Compute[2] the explicit component of the divergence of the current density $^{k}_{h_{\bar{l}},i}$ according to Eq. (3.31).
Compute[2] the stiffness matrix $\mathbb{S}^{h_l,h_{\bar{l}}}$.
Solve the linear system of Eq. (3.37).
Interpolate[2] the electric field at particle positions according to Eq. (3.34).
Advance the particle velocities in time with the implicit contribution of the electric field:

$$\mathbf{v}_p^{k+1} = \mathbf{v}_p^k + \frac{q_p \Delta t}{m_p} \mathbf{E}_{h_n}^{k+1/2}\left(\mathbf{x}_p^{k+1/2}\right).$$

end for

3.2. Properties of the method.

3.2.1. Total energy conservation. In this paper, we derive a scheme that exactly conserves the discrete total energy of the system through time. The discrete total energy comprises the kinetic energy and field energy components. An energy-conserving scheme ensures that changes in kinetic energy, arising from particle velocities, are offset by corresponding changes in field energy, induced by the electric field.

Definition 3.6 (Discrete total energy). *The discrete total energy at time step k, denoted*

[1] It can be done either with finite differences method using the combination technique like in explicit sparse-PIC schemes [13] or with a Galerkin method using the stiffness matrix $\mathbb{K}^{h_l,h_{\bar{l}}}$.

[2] The integral is computed by introducing an approximation of the gradient of the basis functions that is well-defined for all $\boldsymbol{x} \in \Omega$, *e.g.*

$$\int_\Omega \delta\left(\boldsymbol{x} - \boldsymbol{x}_p^{k+\frac{1}{2}}\right) \boldsymbol{\nabla} W_{h_{\bar{l}},i} d\boldsymbol{x} = \int_\Omega \delta\left(\boldsymbol{x} - \boldsymbol{x}_p^{k+\frac{1}{2}}\right) \tilde{\boldsymbol{\nabla}} W_{h_{\bar{l}},i} d\boldsymbol{x} = \tilde{\boldsymbol{\nabla}} W_{h_{\bar{l}},i}\left(\boldsymbol{x}_p^{k+\frac{1}{2}}\right), \tag{3.38}$$

where

$$\tilde{\boldsymbol{\nabla}} W_{h_{\bar{l}},i}(\boldsymbol{x}) = \begin{pmatrix} \tilde{\nabla}_1 W_{h_{\bar{l}},i}(\boldsymbol{x}) \\ \vdots \\ \tilde{\nabla}_d W_{h_{\bar{l}},i}(\boldsymbol{x}) \end{pmatrix}, \quad \tilde{\nabla}_j W_{h_{\bar{l}},i}(\boldsymbol{x}) = \begin{cases} -h_{\bar{l}_j}^{-1} \prod_{\substack{k=1 \\ k\neq j}}^{d} W_{h_{\bar{l}_k},i_k}(x_k) & \text{if } (i_k-1)h_{\bar{l}_k} < x_k < i_k h_{\bar{l}_k}, \\ h_{\bar{l}_j}^{-1} \prod_{\substack{k=1 \\ k\neq j}}^{d} W_{h_{\bar{l}_k},i_k}(x_k) & \text{if } i_k h_{\bar{l}_k} < x_k < (i_k+1)h_{\bar{l}_k}, \\ 0 & \text{else,} \end{cases} \quad , j = 1, \ldots, d. \tag{3.39}$$

by $\mathcal{E}_{\mathcal{T}}^k$, is defined as the sum of the kinetic energy $\mathcal{E}_{\mathcal{K}}^k$ and the field energy $\mathcal{E}_{\mathcal{F}}^k$:

$$\mathcal{E}_{\mathcal{T}}^k := \mathcal{E}_{\mathcal{K}}^k + \mathcal{E}_{\mathcal{F}}^k, \tag{3.40}$$

$$\mathcal{E}_{\mathcal{K}}^k := \frac{1}{2}\sum_{p=1}^{N_s} m_p (\boldsymbol{v}_p^k)^2, \quad \mathcal{E}_{\mathcal{F}}^k := \frac{\varepsilon_0}{2}\int_\Omega |\boldsymbol{E}_{h_n}^k|^2 d\boldsymbol{x} = \frac{\varepsilon_0}{2}\int_\Omega |\boldsymbol{\nabla}\Phi_{h_n}^k|^2 d\boldsymbol{x}. \tag{3.41}$$

THEOREM 3.7 (Exact total energy conservation). *The ECSPIC-2 scheme conserves the total discrete energy exactly:*

$$\mathcal{E}_{\mathcal{T}}^{k+1} = \mathcal{E}_{\mathcal{T}}^k, \quad \forall k \in \mathbb{N}. \tag{3.42}$$

Proof. The changes in kinetic energy between steps $k+1$ and k can be expressed as:

$$\begin{aligned}
\mathcal{E}_{\mathcal{K}}^{k+1} - \mathcal{E}_{\mathcal{K}}^k &= \sum_s \sum_{p=1}^{N_s} \frac{m_p}{2}\left[\left(\boldsymbol{v}_p^{k+1}\right)^2 - \left(\boldsymbol{v}_p^k\right)^2\right] = \sum_s \sum_{p=1}^{N_s} \frac{m_p}{2}\left(\boldsymbol{v}_p^{k+1} + \boldsymbol{v}_p^k\right)\left(\boldsymbol{v}_p^{k+1} - \boldsymbol{v}_p^k\right) \\
&= \Delta t \sum_s \sum_{p=1}^{N_s} \boldsymbol{v}_p^{k+\frac{1}{2}} q_p \boldsymbol{E}_{h_n,N}^{k+\frac{1}{2}}\left(\boldsymbol{x}_p^{k+\frac{1}{2}}\right) \\
&= -\Delta t \sum_{\tilde{\boldsymbol{l}}\in\mathbb{L}^{(1)}} \sum_{\boldsymbol{i}\in\mathcal{B}_{h_{\tilde{\boldsymbol{l}}}}} \hat{\Phi}_{\tilde{\boldsymbol{l}},\boldsymbol{i}}^{k+\frac{1}{2}} \underbrace{\sum_s \sum_{p=1}^{N_s} q_p \boldsymbol{v}_p^{k+\frac{1}{2}} \cdot \left(\int_\Omega \delta\left(\boldsymbol{x} - \boldsymbol{x}_p^{k+\frac{1}{2}}\right)\boldsymbol{\nabla} W_{h_{\tilde{\boldsymbol{l}}},\boldsymbol{i}} d\boldsymbol{x}\right)}_{=_{h_{\tilde{\boldsymbol{l}}},\boldsymbol{i}}^{k+\frac{1}{2}}}.
\end{aligned}$$

Recognizing the source term of the discretized div-Ampere equation, we establish:

$$\begin{aligned}
\mathcal{E}_{\mathcal{K}}^{k+1} - \mathcal{E}_{\mathcal{K}}^k &= -\frac{\varepsilon_0}{2} \sum_{\tilde{\boldsymbol{l}}\in\mathbb{L}^{(1)}} \sum_{\boldsymbol{i}\in\mathcal{B}_{h_{\tilde{\boldsymbol{l}}}}} \left(\hat{\Phi}_{\tilde{\boldsymbol{l}},\boldsymbol{i}}^{k+1} + \hat{\Phi}_{\tilde{\boldsymbol{l}},\boldsymbol{i}}^k\right) \sum_{\boldsymbol{l}\in\mathbb{L}^{(1)}} \sum_{\boldsymbol{j}\in\mathcal{B}_{h_{\boldsymbol{l}}}} (\hat{\Phi}_{\boldsymbol{l},\boldsymbol{j}}^{k+1} - \hat{\Phi}_{\boldsymbol{l},\boldsymbol{j}}^k) \int_\Omega \boldsymbol{\nabla} W_{h_{\tilde{\boldsymbol{l}}},\boldsymbol{i}} \cdot \boldsymbol{\nabla} W_{h_{\boldsymbol{l}},\boldsymbol{j}} d\boldsymbol{x} \\
&= -\left(\frac{\varepsilon_0}{2}\int_\Omega \left[\sum_{\tilde{\boldsymbol{l}}\in\mathbb{L}^{(1)}} \sum_{\boldsymbol{i}\in\mathcal{B}_{h_{\tilde{\boldsymbol{l}}}}} \hat{\Phi}_{\tilde{\boldsymbol{l}},\boldsymbol{i}}^{k+1} \boldsymbol{\nabla} W_{h_{\tilde{\boldsymbol{l}}},\boldsymbol{i}}\right] \cdot \left[\sum_{\boldsymbol{l}\in\mathbb{L}^{(1)}} \sum_{\boldsymbol{j}\in\mathcal{B}_{h_{\boldsymbol{l}}}} \hat{\Phi}_{\boldsymbol{l},\boldsymbol{j}}^{k+1} \boldsymbol{\nabla} W_{h_{\boldsymbol{l}},\boldsymbol{j}}\right] d\boldsymbol{x}\right. \\
&\quad \left. - \frac{\varepsilon_0}{2}\int_\Omega \left[\sum_{\tilde{\boldsymbol{l}}\in\mathbb{L}^{(1)}} \sum_{\boldsymbol{i}\in\mathcal{B}_{h_{\tilde{\boldsymbol{l}}}}} \hat{\Phi}_{\tilde{\boldsymbol{l}},\boldsymbol{i}}^k \boldsymbol{\nabla} W_{h_{\tilde{\boldsymbol{l}}},\boldsymbol{i}}\right] \cdot \left[\sum_{\boldsymbol{l}\in\mathbb{L}^{(1)}} \sum_{\boldsymbol{j}\in\mathcal{B}_{h_{\boldsymbol{l}}}} \hat{\Phi}_{\boldsymbol{l},\boldsymbol{j}}^k \boldsymbol{\nabla} W_{h_{\boldsymbol{l}},\boldsymbol{j}}\right] d\boldsymbol{x}\right) \\
&= -(\mathcal{E}_{\mathcal{F}}^{k+1} - \mathcal{E}_{\mathcal{F}}^k)
\end{aligned}$$

□

Remark 3.8. *A crucial observation is that the field energy defined in Eq. (3.41) is non-negative for all discretizations, i.e., for all approximation spaces $V_h \subset H^1(\Omega)$. Consequently, both the kinetic and field energies are non-negative, ensuring the stability of the scheme. Specifically, since both energy contributions (from particles and the field) remain non-negative, then by induction, the following inequalities hold:*

$$\mathcal{E}_{\mathcal{K}}^k < \mathcal{E}_{\mathcal{T}}^0, \quad \mathcal{E}_{\mathcal{F}}^k < \mathcal{E}_{\mathcal{T}}^0, \quad \forall k \in \mathbb{N}. \tag{3.43}$$

Thus, both the particle velocities and the electric field are bounded by the initial total energy of the system.

3.2.2. Well-posedness and complexity of the linear system. In the previous sections we have introduced a novel semi-implicit scheme in which the implicit contribution of the field is computed by solving a linear system with a stiffness matrix $\mathbb{A}^{h_\iota,h_{\bar{\iota}}} := \mathbb{K}^{h_\iota,h_{\bar{\iota}}} + \mathbb{S}^{h_\iota,h_{\bar{\iota}}}$. Since the discrete space is an approximation of $H^1(\Omega)$, all constant functions are included in the kernel of the Laplacian operator, *i.e.* the Laplacian stiffness matrix $\mathbb{K}^{h_\iota,h_{\bar{\iota}}}$ is not invertible. To address this, we impose a value for the potential at the origin by considering the following modified stiffness matrix:

$$\left(\tilde{\mathbb{K}}^{h_\iota,h_{\bar{\iota}}}_{\boldsymbol{j},\boldsymbol{i}}\right) := \begin{cases} \delta_{\mathbf{0},\boldsymbol{i}}, & \text{if } \boldsymbol{j} = \mathbf{0}, \\ \mathbb{K}^{h_\iota,h_{\bar{\iota}}}_{\boldsymbol{j},\boldsymbol{i}} & \text{else,} \end{cases} \tag{3.44}$$

where $\delta_{\mathbf{0},\boldsymbol{i}}$ is the Kronecker delta symbol, which equals 1 if $\boldsymbol{i} = \mathbf{0}$ and 0 otherwise. By constraining only one value of the potential, the electric field remains unchanged.

Let us recall N_{h_n} the dimension of the sparse grid space, i.e. the size of the linear system discretizing the div-Ampere equation and the size of the stiffness matrix. First, let us assure that the linear system is now well-posed, i.e. the matrix $\tilde{\mathbb{A}}^{h_\iota,h_{\bar{\iota}}} = \tilde{\mathbb{K}}^{h_\iota,h_{\bar{\iota}}} + \mathbb{S}^{h_\iota,h_{\bar{\iota}}}$ is invertible.

Proposition 3.9. *The matrix of the linear system discretizing the div-Ampere equation, denoted $\tilde{\mathbb{A}}^{h_\iota,h_{\bar{\iota}}}$, is a symmetric positive definite matrix and thus invertible.*

Proof. The symmetry property follows directly from the definition. Let $\boldsymbol{\Phi} \in \mathbb{R}^{N_{h_n}}$ be a vector, whose coordinates can be considered as hierarchical coefficients of a function $\Phi_{h_n} \in V^{\mathbb{L}^{(1)}}_{h_n}$. Let $\Psi_{h_n} \in V^{\mathbb{L}^{(1)}}_{h_n}$ be the function with the same hierarchical coefficients as Φ_{h_n}, except the one corresponding to the first level, which is set to zero. The two stiffness matrices $\tilde{\mathbb{K}}^{h_\iota,h_{\bar{\iota}}}$ and $\mathbb{S}^{h_\iota,h_{\bar{\iota}}}$ are positive semi-definite:

$$\begin{aligned} \boldsymbol{\Phi}^T \tilde{\mathbb{K}}^{h_\iota,h_{\bar{\iota}}} \boldsymbol{\Phi} &= \boldsymbol{\Phi}_0^2 + \int_\Omega \left(\sum_{\substack{\boldsymbol{l} \in \mathbb{L}^{(1)} \\ \boldsymbol{l} \neq \mathbf{0}}} \sum_{\boldsymbol{j} \in \mathcal{B}_{h_\iota}} \Phi_{\boldsymbol{l},\boldsymbol{j}} \boldsymbol{\nabla} W_{h_\iota,\boldsymbol{j}} \right) \cdot \left(\sum_{\substack{\bar{\boldsymbol{l}} \in \mathbb{L}^{(1)} \\ \bar{\boldsymbol{l}} \neq \mathbf{0}}} \sum_{\boldsymbol{i} \in \mathcal{B}_{h_{\bar{\iota}}}} \Phi_{\bar{\boldsymbol{l}},\boldsymbol{i}} \boldsymbol{\nabla} W_{h_{\bar{\iota}},\boldsymbol{i}} \right) d\boldsymbol{x} \\ &= \boldsymbol{\Phi}_0^2 + \int_\Omega \left| \boldsymbol{\nabla} \Psi_{h_n} \right|^2 d\boldsymbol{x} \geq 0, \end{aligned}$$

and

$$\begin{aligned} &\boldsymbol{\Phi}^T \mathbb{S}^{h_\iota,h_{\bar{\iota}}} \boldsymbol{\Phi} = \\ &\sum_s \sum_{p=1}^{N_s} \frac{q_p^2 \Delta t^2}{2 m_p \varepsilon_0} \int_\Omega \left(\sum_{\boldsymbol{l} \in \mathbb{L}^{(1)}} \sum_{\boldsymbol{j} \in \mathcal{B}_{h_\iota}} \Phi_{\boldsymbol{l},\boldsymbol{j}} \boldsymbol{\nabla} W_{h_\iota,\boldsymbol{j}} \right) \cdot \left(\sum_{\bar{\boldsymbol{l}} \in \mathbb{L}^{(1)}} \sum_{\boldsymbol{i} \in \mathcal{B}_{h_{\bar{\iota}}}} \Phi_{\bar{\boldsymbol{l}},\boldsymbol{i}} \boldsymbol{\nabla} W_{h_{\bar{\iota}},\boldsymbol{i}} \right) \delta\left(\boldsymbol{x} - \boldsymbol{x}_p^{k+\frac{1}{2}} \right) d\boldsymbol{x} \\ &= \sum_s \sum_{p=1}^{N_s} \underbrace{\frac{q_p^2 \Delta t^2}{2 m_p \varepsilon_0}}_{>0} \int_\Omega \left| \boldsymbol{\nabla} \Phi_{h_n} \right|^2 \delta\left(\boldsymbol{x} - \boldsymbol{x}_p^{k+\frac{1}{2}} \right) d\boldsymbol{x} \geq 0. \end{aligned}$$

Let us now prove that the modified Laplacian stiffness matrix $\tilde{\mathbb{K}}^{h_\iota,h_{\bar{\iota}}}$ is positive definite. We assume that:

$$\boldsymbol{\Phi}^T \tilde{\mathbb{K}}^{h_\iota,h_{\bar{\iota}}} \boldsymbol{\Phi} = \boldsymbol{\Phi}_0^2 + \int_\Omega \left| \boldsymbol{\nabla} \Psi_{h_n} \right|^2 d\boldsymbol{x} = 0.$$

Then it follows:

$$\boldsymbol{\Phi}_0 = 0, \quad \boldsymbol{\nabla} \Psi_{h_n}(\boldsymbol{x}) = 0, \ \ \forall \boldsymbol{x} \in \Omega,$$

and since $\Psi_{h_n}(\mathbf{0}) = 0$, $\Psi_{h_n} \equiv 0$ and thus $\boldsymbol{\Phi}_i = 0, i = 1, ..., N_{h_n}$. ∎

One of the advantages of semi-implicit methods over explicit methods, is the significant gain achieved by enabling larger time steps and coarser mesh discretization without causing numerical instability. However, this comes at the cost of increased computational complexity due to the necessity of solving a linear system at each iteration, with the matrix needing to be recomputed each time. Sparse grid discretization aims to alleviate these computational burdens. In the following section, we provide insights into the potential benefits offered by the hierarchical sparse grid discretization of our newly introduced scheme, in comparison to standard discretizations and sparse grid discretizations based on the combination technique. Let us denote the sizes of the linear systems corresponding to the SISPIC-sg [21] (which is similar to the SISPIC-std [21] and ECSIM [29] schemes), ECSPIC-1 [21], and ECSPIC-2 schemes, respectively, as follows:

$$N_{h_n}^{SIS} = h_n^{-d}, \quad N_{h_n}^{ECS1} = \sum_{r=0}^{d-1} \frac{2^{d-1-r}}{(d-1)!} \frac{(n+d-2-r)!}{(n-1-r)!} h_n^{-1}, \tag{3.45}$$

$$N_{h_n}^{ECS2} = \frac{n^{d-1}}{(d-1)!} h_n^{-1} + O\left(|\log h_n|^{d-2}\right). \tag{3.46}$$

While the linear system sizes for the two energy-conserving schemes are of the same order, specifically $O\left(h_n^{-1}|\log h_n|^{d-1}\right)$, the constants in their estimations differ. Consequently, the ECSPIC-2 scheme shall yield a significantly smaller system size compared to the ECSPIC-1 scheme (see Fig. 1). This characteristic, which becomes more pronounced in three dimensions, highlights the advantages conferred by the hierarchical sparse grid representation over the combination technique.

4. Numerical results. In this section, we aim to demonstrate the conservation and stability properties of the scheme introduced in this paper, as well as establish its validity through a series of classical test cases. Specifically, we examine two numerical test cases: (weak and strong) Landau damping and two-stream instability. Our method is compared to existing PIC schemes, including the explicit standard (Exp-std) and sparse (Exp-sg) PIC schemes, and the semi-implicit sparse-PIC schemes (SISPIC-sg and ECSPIC-1) introduced in [21].

All subsequent simulations are conducted on a laptop equipped with an Apple M2 CPU and 24GB of RAM. The linear systems are solved using the DGESV routine from LAPACK library [15].

Although the benefits of sparse grid methods are more pronounced in three-dimensional computations, we have implemented these methods in two spatial dimensions and three velocity dimensions (2d-3v) for preliminary evaluation. In this study, we do not provide direct comparisons of computational time between the newly introduced method and existing ones, as a fair comparison would necessitate optimizations tailored to each method. For instance, we utilize a dense linear algebra library (LAPACK) for all schemes, which is particularly advantageous for handling the dense linear systems of sparse grid schemes compared to the sparse linear systems of standard grid schemes.

The domain is a periodic square $\Omega = (\mathbb{R}/L\mathbb{Z})^2$, of dimension $L \in \mathbb{R}_+^*$. Dimensionless variables are considered, the reference length and time units being the Debye length and the plasma period, defined by:

$$\lambda_D = \sqrt{\varepsilon_0 T_e / q_e n_0}, \qquad \omega_p^{-1} = 1/\sqrt{q_e n_0 / m_e \varepsilon_0}. \tag{4.1}$$

The electrons are considered immersed in a uniform, immobile, background of ions. Electron mass, temperature and charge are normalized to one. Periodic boundary conditions are considered for the particles and the field.

The results are compared without any filtering methods for all schemes. The momentum error in the simulation at iteration k is measured by the sum of the momentum error vector:

$$\varepsilon_{\mathcal{M}}^{k} := \left| \sum_{r=1}^{d} \left(\sum_{s} \frac{1}{N_s} \sum_{p=1}^{N_s} \frac{m_s \mathbf{v}_p^k - m_s \mathbf{v}_p^0}{m_s v_T} \right)_r \right|, \tag{4.2}$$

where $v_T := \sqrt{2q_s T_s / m_s}$ is the thermal velocity of the electrons. The total discrete energy error at time iteration k is defined by:

$$\varepsilon_{\mathcal{E}}^{k} := \left| \sum_{r=1}^{d} \left(\frac{\mathcal{E}_{\mathcal{K}}^k + \mathcal{E}_{\mathcal{F}}^k - \left(\mathcal{E}_{\mathcal{K}}^0 + \mathcal{E}_{\mathcal{F}}^0 \right)}{\mathcal{E}_{\mathcal{K}}^0 + \mathcal{E}_{\mathcal{F}}^0} \right)_r \right|, \tag{4.3}$$

where $\mathcal{E}_{\mathcal{K}}^k$ and $\mathcal{E}_{\mathcal{F}}^k$ are the kinetic and field energy measured at time k.

Throughout this section, we will refer to the mean number of particles per cell, denoted P_c, relating the amount of statistical noise in the simulation. It is defined by:

$$P_c = N_e N_{c,h_n}^{-1}, \tag{4.4}$$

where N_e is the total number of particles (i.e. electrons) and N_{c,h_n} is the total number of grid cells. For the Exp-std, and ECSPIC-1 schemes, this quantity corresponds to the size of the linear system, denoted by N_{h_n} and defined in Eq. (3.45). For the Exp-sg and SISPIC-sg it is defined by:

$$N_{c,h_n}^{sg} = \sum_{\sigma=0}^{d-1} \sum_{|\boldsymbol{l}|_1 = n+d-1-\sigma} h_{l_1}^{-1} \dots h_{l_d}^{-1}, \tag{4.5}$$

and for the ECSPIC-2 scheme, it is defined by:

$$N_{c,h_n}^{ECS2} = \sum_{\boldsymbol{l} \in \mathbb{L}^{(1)}} h_{l_1}^{-1} \dots h_{l_d}^{-1}. \tag{4.6}$$

4.1. Finite grid instability. The phenomenon known as aliasing or finite grid instability, initially examined in [27], is a prevalent numerical instability encountered in PIC plasma simulations. This instability arises from the discrepancy between the discrete Eulerian grid discretization of the fields and the continuous phase-space discretization of Lagrangian particles [24].

In simulations, this instability manifests as numerical heating of the plasma [2], influenced by numerical parameters. As aliasing introduces artificial heat into the system, it is also characterized by a violation of energy conservation. To mitigate aliasing instability, PIC simulations typically employ a grid discretization that is equal to or smaller than the Debye length ($h_n \leq \lambda_D$), even for problems where the scales of interest are significantly larger than the Debye length. For instance, dense plasmas are adequately described by the quasi-neutral approximation in most regions, and simulating plasma physics does not require grid cells smaller than the Debye length. Consequently, substantial benefits could be realized with coarser grid cells that do not resolve the Debye length, particularly in three-dimensional computations.

In this section, we aim to numerically establish that the introduced ECSPIC-2 scheme do not exhibit finite grid instability in classical configurations where an explicit discretization

does. We consider an initially Maxwellian and stable plasma with the following electron distribution:

$$f_v^0(\mathbf{v}) = \left(\frac{1}{\sqrt{\pi} v_T}\right)^3 e^{-\|\mathbf{v}\|_2^2 / v_T^2}, \tag{4.7}$$

where $v_T = \sqrt{2T_e q_e / me}$ is the thermal velocity of electrons and $\|\mathbf{v}\|_2^2 = v_1^2 + v_2^2 + v_3^2$. The size of the domain is $L = 5\pi, 15\pi, 50\pi$ and the grid discretization is $h_n = 2^{-5}L$. Some of these configurations (the two lasts) shall lead to the development of the finite-grid instability for the explicit schemes, since the grid discretization is larger than the Debye length. The first dimension of the particle phase space (x_1, v_1) is represented at time $T = 200$ on Fig. 2 for the standard explicit scheme and the ECSPIC-2 scheme, in various configurations of the domain.

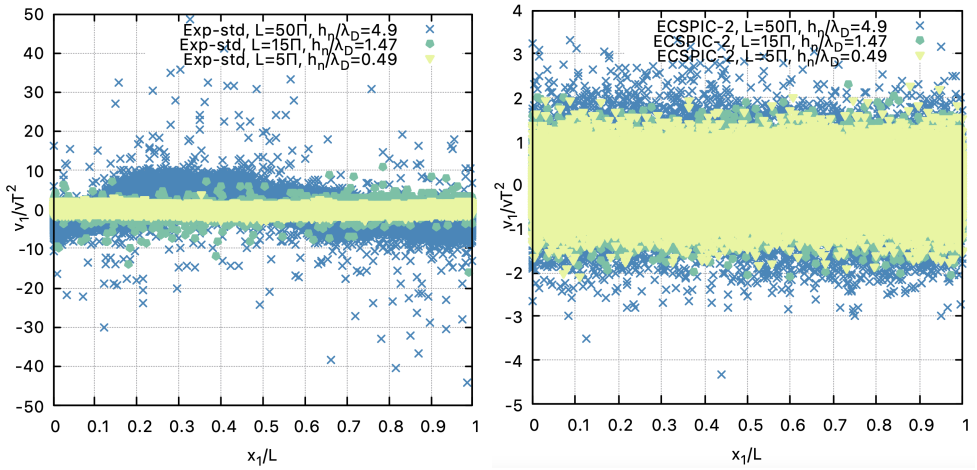

Fig. 2: Finite-grid instability: representation of the phase space (x_1, v_1) of an initially Maxwellian distribution of electrons at time $T = 200$. $P_c = 100$, $\Delta t = 0.05$ for the explicit scheme and $\Delta t = 0.5$ for the ECSPIC-2 scheme.

The finite grid instability is apparent in the explicit scheme when the grid discretization exceeds the Debye length: the particle velocities increase, leading to a rise in the system's total energy. We observe that the ECSPIC-2 scheme is free from finite grid instability in configurations where the explicit scheme demonstrates instability. As noted in Remark 3.8, this stability is guaranteed by the exact conservation of energy and the non-negativity of both kinetic and field energy, which ensure that the velocities and field energy remain bounded by the initial total energy.

4.2. Landau damping.

4.2.1. Weak damping. The first test case examined is the well-known phenomenon of Landau damping [26, 25]. When a plasma is slightly perturbed from its equilibrium state, it returns to equilibrium through exponential damping. For this test, we consider a slight perturbation in the electron distribution from an equilibrium state:

$$f_e(\mathbf{x}, \mathbf{v}, 0) = f_v^0(\mathbf{v}) f_x^0(\mathbf{x}), \tag{4.8}$$

where the initial velocity distribution is Maxwellian, similar to the previous configuration defined by Eq. (4.7), and the perturbation has the following form:

$$f_x^0(\mathbf{x}) = (1 + \alpha_1 \cos(k_1 x_1))\,(1 + \alpha_2 \cos(k_2 x_2))\,. \tag{4.9}$$

$\boldsymbol{\alpha}$ is the magnitude and $\mathbf{k}$ is the period of the perturbation. The perturbation is considered uniform in each dimension, *i.e.* $k_i = k$, $k \in \mathbb{R}$ and the domain size depends on the perturbation:

$$L = \frac{2\pi}{k}. \tag{4.10}$$

By considering the roots of the dispersion function ($\varepsilon(\omega, k) = 0$), which is as follows:

$$\frac{1}{\varepsilon_0}\varepsilon(\omega, k) = 1 + \frac{1}{k^2}\left(1 + \frac{\omega}{\sqrt{2}k} Z\left(\frac{\omega}{\sqrt{2}k}\right)\right), \tag{4.11}$$

one can find the damping rate of the plasma ($\Im(\omega)$) for given values of $k \in \mathbb{R}$ [2]. *E.g.* for $k = 0.3$, the root with the largest imaginary part is $\omega = \pm 1.1598 - 0.0126i$, etc.

Let us parametrize the perturbation with $\alpha_1 = \alpha_2 = 0.05$, $k = 0.3$ such that the domain size is $L = 20\pi/3$. The final time is $T = 50$. The grid discretization is $h_n = 2^{-5}L$ so that the Debye length is resolved: $h_n \approx 0.65\lambda_D$.

The evolution of the electric field L^2-norm in time is provided on the panels of Fig. 4 for different configurations described in Fig. 3. The evolution of the total energy error in time is also provided on the bottom right panel of Fig. 4. For the ECSPIC-1 scheme, the L^2-norm of the electric field is computed on the Cartesian grid after combination of the field. An expensive standard explicit simulation with $\Delta t = 0.01\omega_p^{-1}$ and $P_c = 5,000$ is chosen as a reference and compared to the sparse grid semi-implicit schemes with a larger time step ranging from $\Delta t = 0.1\omega_p^{-1}$ to $\Delta t = 1\omega_p^{-1}$ and fewer particles per cell $P_c = 500$. We observe, as highlighted in [21], that the ECSPIC-1 scheme is numerically instable, leading to an increase of the total energy and total momentum error in time. The ECSPIC-2 is exempted from this numerical instability thanks to the non-negative field energy involved in the total energy conservation. Out of the three semi-implicit sparse grid schemes, the ECSPIC-2 is the one providing results that suit the best the reference solution. The theoretical rate of damping is matched for all Δt. The ECSPIC-2 scheme also offers a significant reduction in grid complexity. The size of the linear system (N_{h_n}) to solve is reduced by a factor of 4 compared to the ECSPIC-1 scheme and by a factor of approximately 10 compared to the SISPIC-sg scheme. The total energy is exactly, up to machine precision, conserved for the ECSPIC-2 scheme as proved by Theorem 3.7. Additionally, the total momentum error remains around 1E−04.

4.2.2. Strong damping. When the perturbation of the equilibrium state is considered large enough to invalidate the linear approximation, the previous analytic damping rate is not available anymore. In order to assess the efficiency of the method, the results are compared to a reference solution computed with a high-resolution simulation performed with the Exp-std scheme. This reference solution is considered with $\Delta t = 0.01$, $P_c = 10,000$ and $h_n = 2^{-6}$.

Let us parametrize the perturbation with $\alpha_1 = \alpha_2 = 0.2$, $k = 3$ and the domain size is $L = 60$. The final time is $T = 5.5$. The grid discretization has to be at least $h_n = 2^{-6}L$ for the Exp-std scheme so that the Debye length is resolved: $h_n \approx 0.938\lambda_D$. Fig. 5 presents the evolution of the electric field L^2-norm over time for various configurations of the different schemes, as summarized in the table within the same figure. Additionally, Fig. 6 provides a representation of the electric potential interpolated at the standard grid at time $t = 2.9$. As observed in Fig. 5, the ECSPIC-2 scheme closely aligns with the reference solution for all Δt values, similar to the SISPIC-sg scheme, while the Exp-std scheme fails to accurately

Table 3: Landau damping (weak damping): configurations of the simulations (Fig. 4), $k = 0.3$.

scheme	Δt	h_n	N_{h_n} (% of nonzero)	P_c	N_e	color
Ex-std (ref)	0.01	2^{-5}	1,024 (2.1%)	5,000	2.5E+06	
SISPIC-sg	0.1; 0.5; 1	2^{-5}	1,024 (2.1%)	500	2.24E+05	
ECSPIC-1	0.1; 0.5; 1	2^{-5}	448 (56.4%)	500	2.24E+05	
ECSPIC-2	0.1; 0.5; 1	2^{-5}	112 (39.7%)	500	1.6E+05	

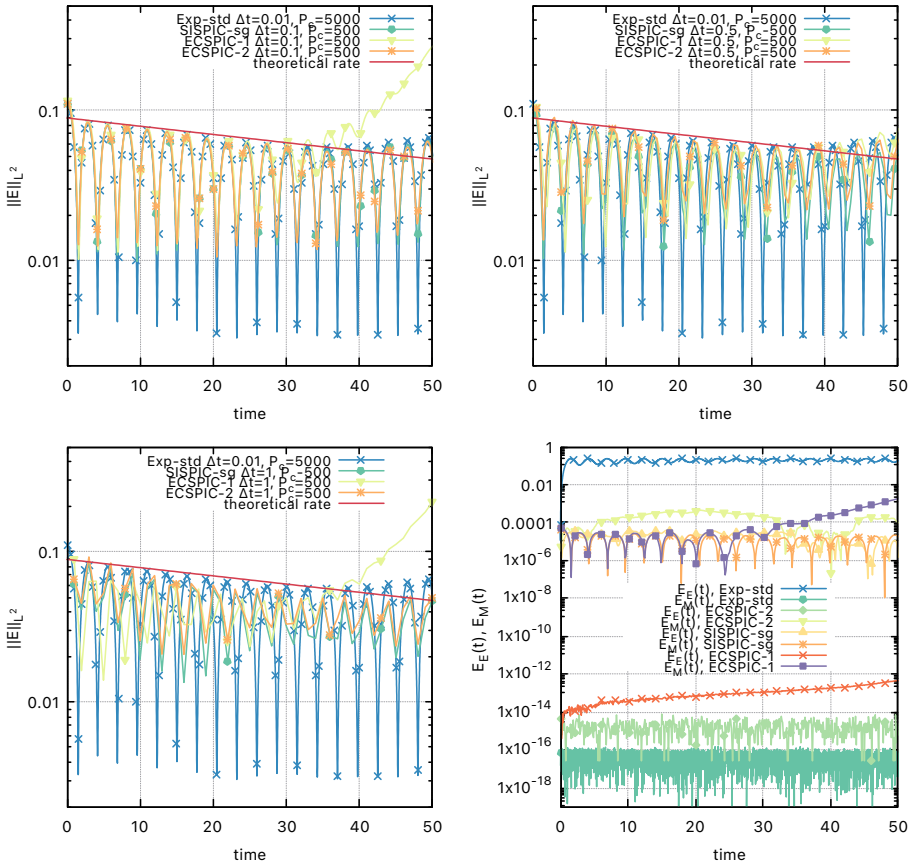

Fig. 4: Landau damping (weak damping): evolution of the electric field L^2-norm $\|\mathbf{E}_h\|_{L^2}$ in time for different time steps Δt, $k = 0.3$(*cf.* Fig. 3). Evolution of the total energy error $\epsilon_{\mathcal{E}}(t)$ and total momentum error $\epsilon_{\mathcal{M}}(t)$ in time (bottom right panel), corresponding to the top left panel simulation.

reproduce the oscillation periods for larger Δt. Additionally, the ECSPIC-1 scheme performs slightly less effectively than the ECSPIC-2 scheme in these configurations. Fig. 5 also demonstrates that the ECSPIC-2 scheme achieves a reasonable approximation of the electric potential with significantly fewer grid nodes and particles compared to the standard scheme.

scheme	h_n	N_{h_n} (% of nonzero)	Δt	P_c	N_e	color
Ex-std (ref)	2^{-6}	4,096 (0.12%)	0.01	10,000	4.1E+07	■
Ex-std	2^{-6}	4,096 (0.12%)	0.1	500	2.0E+06	■
Ex-std	2^{-6}	4,096 (0.12%)	0.5	500	2.0E+06	■
ECSPIC-1	2^{-6}	1,088 (40.8%)	0.1	500	5.4E+05	■
ECSPIC-1	2^{-5}	448 (56.4%)	0.5	500	2.2E+05	■
SISPIC-sg	2^{-6}	4,096 (0.5%)	0.1	500	5.4E+05	■
SISPIC-sg	2^{-5}	1,024 (2.0%)	0.5	500	2.2E+05	■
ECSPIC-2	2^{-6}	256 (33.6%)	0.1	500	3.8E+05	■
ECSPIC-2	2^{-5}	112 (39.7%)	0.5	500	1.6E+05	■

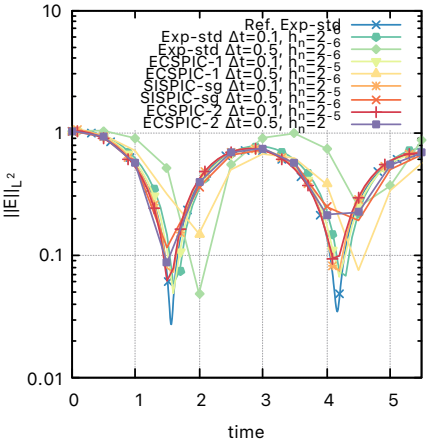

Fig. 5: Landau damping (strong damping): evolution of the electric field L^2-norm $\|\mathbf{E}_h\|_{L^2}$ in time (right panel). Different configurations considered (left table).

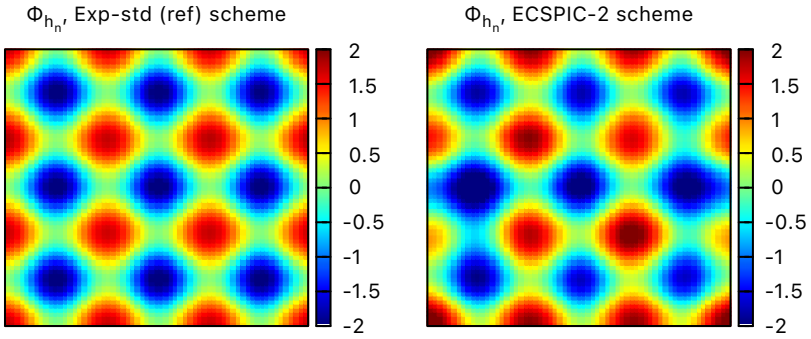

Fig. 6: Landau damping (strong damping): Electric potential interpolated at the standard grid at time $t = 2.9$. Exp-std scheme: $\Delta t = 0.01$, $P_c = 10,000$, $h_n = 2^{-6}$ (left panel; ■ on Fig. 5). ECSPIC-2 scheme: $\Delta t = 0.1$, $P_c = 500$, $h_n = 2^{-6}$ (right panel; ■ on Fig. 5).

4.3. Two-streams instability. The two-stream instability configuration, as described by [1], involves two particle beams moving with opposite mean velocities. The initial electron distribution is given by a Maxwellian distribution:

$$f_e(\mathbf{x}, \mathbf{v}, 0) = f_v^0(\mathbf{v}) f_x^0(\mathbf{x}), \tag{4.12}$$

where the perturbation has a similar form to that of Landau damping, and the initial velocity distribution comprises two beams:

$$f_v^0(\mathbf{v}) = \left(\frac{1}{\sqrt{\pi} v_T}\right)^2 \left(e^{\frac{-\|\mathbf{v}-\mathbf{v}_0\|_2^2}{v_T^2}} + e^{\frac{-\|\mathbf{v}+\mathbf{v}_0\|_2^2}{v_T^2}} \right). \tag{4.13}$$

$\mathbf{v}_0 = (v_0, 0) \in \mathbb{R}^2$ is the mean velocity of the beams in opposite direction and the domain size is:

$$L = \frac{2\pi}{k}, \tag{4.14}$$

where $k_i = k \in \mathbb{R}$, for $i = 1, 2$. Depending on the values of k and v_0, the configuration can be either stable or unstable. When the two streams pass through each other in such a way that one wavelength is traveled in one cycle of the plasma frequency, the perturbation from one stream amplifies the perturbation in the other, causing the perturbation to grow exponentially over time. The linear dispersion relation for this test case is:

$$\frac{1}{\varepsilon_0}\varepsilon(\omega, \mathbf{k}) = 1 - \frac{\omega_p^2}{(\omega - \mathbf{k}\cdot\mathbf{v}_0)^2} - \frac{\omega_p^2}{(\omega + \mathbf{k}\cdot\mathbf{v}_0)^2}. \tag{4.15}$$

The four roots of the linear dispersion relation are [2]:

$$\omega = \pm\left[k^2 v_0^2 + \omega_p^2 \pm \omega_p\left(4k^2 v_0^2 + \omega_p^2\right)^{\frac{1}{2}}\right]^{\frac{1}{2}}, \tag{4.16}$$

which can be imaginary, and lead to instability, for:

$$0 \le \frac{k v_0}{\omega_p} \le \sqrt{2}. \tag{4.17}$$

Let us parametrize the perturbation with $\alpha_1 = \alpha_2 = 0.005$, $k = 0.05$ such that the domain size is $L = 40\pi$. The mean velocity is $v_0 = 12$ and the final time $T = 70$. The grid discretization is $h_n = 2^{-5}L$ for the semi-implicit schemes and $h_n = 2^{-7}L$ for the explicit scheme to ensure the Debye length is resolved, yielding $h_n \approx 0.98\lambda_D$. To reduce computational costs, we employ the sparse-PIC explicit scheme as a comparison to semi-implicit schemes. It is considered with $\Delta t = 0.01$, $P_c = 1,000$ and $h_n = 2^{-7}$.

Fig. 7 presents the evolution of the electric field L^2-norm over time for various configurations summarized in the table on the left panel. All schemes adhere to the theoretical growth rate. It is notable that the ECSPIC-1 scheme exhibits instability in this test case, whereas the ECSPIC-2 scheme remains stable.

scheme	h_n	N_{h_n} (% of nonzero)	Δt	P_c	N_e	color
Ex-sg	2^{-7}	7 of 256 (1.9%) 6 of 128 (3.9%)	0.01	1,000	2.6E+06	
SISPIC-sg	2^{-5}	1,024 (2.0%)	0.1	500	2.2E+05	
ECSPIC-1	2^{-5}	448 (56.4%)	0.1	500	2.2E+05	
ECSPIC-2	2^{-5}	112 (39.7%)	0.1	500	1.6E+05	

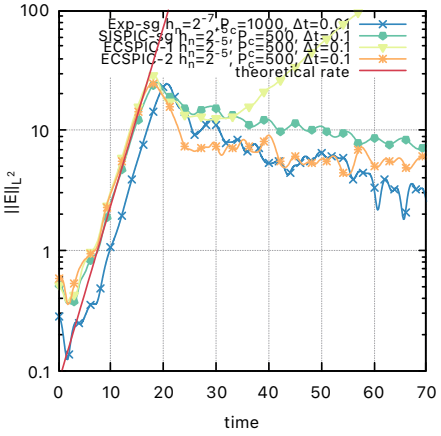

Fig. 7: Two-streams instability: evolution of the electric field L^2-norm $\|\mathbf{E}_h\|_{L^2}$ in time for different schemes, $k = 0.05$, $v_0 = 12$, $\Delta t = 0.1$, $P_c = 500$.

5. Conclusion. This paper introduces a novel numerical method, the ECSPIC-2 scheme, based on an implicit discretization of the Vlasov-Maxwell system in the electrostatic regime,

incorporating sparse grids to exactly conserve discrete total energy. By employing a weak formulation of the div-Ampere equation, a non-negative field energy is defined. The scheme ensures exact conservation of total energy, including non-negative kinetic and field energies, thereby ensuring stability. This represents a significant improvement over existing semi-implicit schemes with sparse grids, which do not guarantee exact energy conservation and stability simultaneously. The method incorporates all advantages of existing semi-implicit PIC schemes, summarized in Table 1. Moreover, the hierarchical sparse grid representation of basis functions reduces the complexity of the linear system to solve compared to existing sparse grid semi-implicit schemes (SISPIC-sg and ECSPIC-1).

Acknowledgements. The author would like to acknowledge useful discussions with F. Deluzet and J. Narski.
This work has been carried out within the framework of the EUROfusion Consortium, funded by the European Union via the Euratom Research and Training Programme (Grant Agreement No 101052200 — EUROfusion). Views and opinions expressed are however those of the author only and do not necessarily reflect those of the European Union or the European Commission. Neither the European Union nor the European Commission can be held responsible for them.
This work has been supported by a public grant from the "Laboratoire d'Excellence Centre International de Mathématiques et d'Informatique" (LabEx CIMI) overseen by the French National Research Agency (ANR) as part of the "Investissements d'Avenir" program (reference ANR-11-LABX-0040) in the frame of the PROMETEUS project (PRospect of nOvel nuMerical modEls for elecTric propulsion and low tEmperatUre plaSmas).
This work has been supported by a grant from the French National Research Agency (ANR) project MATURATION (reference ANR-22-CE46-0012)
Support from the FrFCM (Fédération de recherche pour la Fusion par Confinement Magnétique) in the frame of the SPARCLE project (SParse grid Acceleration for the paRticle-in-CelL mEthod) and the BRIDIPIC project "BRIDging Particle-In-Cell methods and low frequency numerical models of plasmas" is also acknowledged.

References.

[1] C.K. Birdsall. *Interaction Between Two Electron Streams for Microwave Amplification*. Department of Electrical Engineering, Stanford University, 1951.
[2] C.K. Birdsall and A.B Langdon. *Plasma Physics via Computer Simulation*. CRC Press, October 2018.
[3] J.U. Brackbill. On energy and momentum conservation in particle-in-cell plasma simulation. *Journal of Computational Physics*, 317:405–427, July 2016.
[4] J.U Brackbill and D.W Forslund. An implicit method for electromagnetic plasma simulation in two dimensions. *Journal of Computational Physics*, 46(2):271–308, May 1982.
[5] G. Chen and L. Chacón. A multi-dimensional, energy- and charge-conserving, nonlinearly implicit, electromagnetic Vlasov–Darwin particle-in-cell algorithm. *Computer Physics Communications*, 197:73–87, December 2015.
[6] Bruce I Cohen, A.Bruce Langdon, and A Friedman. Implicit time integration for plasma simulation. *Journal of Computational Physics*, 46(1):15–38, August 1982.
[7] Lars K.S. Daldorff, Gábor Tóth, Tamas I. Gombosi, Giovanni Lapenta, Jorge Amaya, Stefano Markidis, and Jeremiah U. Brackbill. Two-way coupling of a global Hall magnetohydrodynamics model with a local implicit particle-in-cell model. *Journal of Computational Physics*, 268:236–254, July 2014.
[8] John M. Dawson. Particle simulation of plasmas. *Rev. Mod. Phys.*, 55(2):403–447, April 1983. Publisher: American Physical Society.

[9] Pierre Degond, Fabrice Deluzet, and David Doyen. Asymptotic-preserving Particle-In-Cell methods for the Vlasov-Maxwell system near quasi-neutrality. *arXiv:1509.04235 [physics]*, September 2015. arXiv: 1509.04235.

[10] F. Deluzet, G. Fubiani, L. Garrigues, C. Guillet, and J. Narski. Efficient parallelization for 3d-3v sparse grid particle-in-cell: shared memory architectures. Submitted to Journal of Computational physics, 2022.

[11] F. Deluzet, G. Fubiani, L. Garrigues, C. Guillet, and J. Narski. Efficient parallelization for 3d-3v sparse grid particle-in-cell: Single gpu architectures. Submitted to Computer Physics Communications, 2022.

[12] F. Deluzet, C. Guillet, J. Narski, and P. Pace. High-order sparse-pic methods: analysis and numerical investigations. Submitted to SIAM:SINUM.

[13] Fabrice Deluzet, Gwenael Fubiani, Laurent Garrigues, Clément Guillet, and Jacek Narski. Sparse grid reconstructions for Particle-In-Cell methods. *ESAIM: M2AN*, 56(5):1809–1841, September 2022.

[14] J Denavit and JM Walsh. Proceedings of the ninth conference on numerical simulation of plasmas. *J. Comput. Phys*, 42:337, 1981.

[15] Anderson E., Bai Z., Bischof C., Blackford S., Demmel J., Dongarra J., Du Croz J., Greenbaum A., Hammarling S., McKenney A., and Sorensen D. *LAPACK Users' Guide*. Society for Industrial and Applied Mathematics, 1999.

[16] L. Garrigues, B. Tezenas du Montcel, G. Fubiani, F. Bertomeu, F. Deluzet, and J. Narski. Application of sparse grid combination techniques to low temperature plasmas particle-in-cell simulations. I. Capacitively coupled radio frequency discharges. *Journal of Applied Physics*, 129(15):153303, April 2021. Publisher: American Institute of Physics.

[17] L. Garrigues, B. Tezenas du Montcel, G. Fubiani, and B. C. G. Reman. Application of sparse grid combination techniques to low temperature plasmas Particle-In-Cell simulations. II. Electron drift instability in a Hall thruster. *Journal of Applied Physics*, 129(15):153304, April 2021. Publisher: American Institute of Physics.

[18] Laurent Garrigues, Gwénaël Fubiani, and Jean-Pierre Boeuf. Negative ion extraction via particle simulation for fusion: critical assessment of recent contributions. *Nuclear Fusion*, 57(1):014003, January 2017. Publisher: IOP Publishing.

[19] Laurent Garrigues, Marc Chung To Sang, Gwenael Fubiani, Clement Guillet, Fabrice Deluzet, and Jacek Narski. Acceleration of particle-in-cell simulations using sparse grid algorithms.i. application to dual frequency capacitive discharges. Submitted to Physics of Plasmas.

[20] Laurent Garrigues, Marc Chung To Sang, Gwenael Fubiani, Clement Guillet, Fabrice Deluzet, and Jacek Narski. Acceleration of particle-in-cell simulations using sparse grid algorithms.ii. application to partially magnetized low temperature plasmas. Submitted to Physics of Plasmas.

[21] C. Guillet. Semi-implicit particle-in-cell methods embedding sparse grid reconstructions. *Multiscale Modeling and Simulation*, 22(2):891–924, June 2024.

[22] Markus Hegland, Giles Hooker, and Stephen Roberts. Finite element thin plate splines in density estimation. *ANZIAM Journal*, 42:712, July 2009.

[23] Dennis W Hewett and A Bruce Langdon. Electromagnetic direct implicit plasma simulation. *Journal of Computational Physics*, 72(1):121–155, 1987.

[24] C.-K. Huang, Y. Zeng, Y. Wang, M.D. Meyers, S. Yi, and B.J. Albright. Finite grid instability and spectral fidelity of the electrostatic Particle-In-Cell algorithm. *Computer Physics Communications*, 207:123–135, October 2016.

[25] Nicholas A. Krall and Alvin W. Trivelpiece. Principles of Plasma Physics. *American Journal of Physics*, 41(12):1380–1381, December 1973. Publisher: American Association of Physics Teachers.

[26] L. Landau. On the vibrations of the electronic plasma. *Journal of Physics*, 1945.
[27] A.Bruce Langdon. Effects of the spatial grid in simulation plasmas. *Journal of Computational Physics*, 6(2):247–267, October 1970.
[28] A.Bruce Langdon, Bruce I Cohen, and Alex Friedman. Direct implicit large time-step particle simulation of plasmas. *Journal of Computational Physics*, 51(1):107–138, 1983.
[29] Giovanni Lapenta. Exactly energy conserving semi-implicit particle in cell formulation. *Journal of Computational Physics*, 334:349–366, April 2017.
[30] Rodney J Mason. Implicit moment particle simulation of plasmas. *Journal of Computational Physics*, 41(2):233–244, June 1981.
[31] Sriramkrishnan Muralikrishnan, Antoine J. Cerfon, Matthias Frey, Lee F. Ricketson, and Andreas Adelmann. Sparse grid-based adaptive noise reduction strategy for particle-in-cell schemes. *Journal of Computational Physics: X*, 11:100094, June 2021.
[32] Benjamin Peherstorfer, Dirk Pflüger, and Hans-Joachim Bungartz. *Density Estimation with Adaptive Sparse Grids for Large Data Sets*. 01 2017.
[33] L F Ricketson and A J Cerfon. Sparse grid techniques for particle-in-cell schemes. *Plasma Phys. Control. Fusion*, 59(2):024002, February 2017.
[34] Gábor Tóth, Yuxi Chen, Tamas I. Gombosi, Paul Cassak, Stefano Markidis, and Ivy Bo Peng. Scaling the Ion Inertial Length and Its Implications for Modeling Reconnection in Global Simulations. *JGR Space Physics*, 122(10), October 2017.
[35] Gábor Tóth, Xianzhe Jia, Stefano Markidis, Ivy Bo Peng, Yuxi Chen, Lars K. S. Daldorff, Valeriy M. Tenishev, Dmitry Borovikov, John D. Haiducek, Tamas I. Gombosi, Alex Glocer, and John C. Dorelli. Extended magnetohydrodynamics with embedded particle-in-cell simulation of Ganymede's magnetosphere. *J. Geophys. Res. Space Physics*, 121(2):1273–1293, February 2016.